ACS Catalysis

pubs.acs.org/acscatalysis Research Article

# Hydrogenation of Alkenes, Cycloalkenes, and Arene Side Chains at Lewis Acid–Base Pairs: Kinetics, Elementary Steps, and Thermodynamic Implications for Reverse Reactions

Nicholas R. Jaegers, Mikalai Artsiusheuski, Vardan Danghyan, Junnan Shangguan, Carlos Lizandara-Pueyo, and Enrique Iglesia*

Cite This: ACS Catal. 2025, 15, 12610–12626 Read Online

ACCESS | Metrics & More | Article Recommendations | Supporting Information

**ABSTRACT:** Hydrocarbon hydrogenation reactions are prevalent routes to essential chemical intermediates. Lewis acid–base (LAB) site pairs on earth-abundant *m*-$ZrO_2$ are competent active sites for the hydrogenation of ethene, propene, cyclopentene, and styrene. Chemical treatments with dimethyl ether remove strongly bound titrants ($H_2O$, $CO_2$) from LAB sites and uncover the most competent low-coordination Zr–O pairs at much lower temperatures than treatments that induce thermal desorption, leading to 30–100-fold enhancements of hydrogenation rates. These treatments render earth-abundant *m*-$ZrO_2$ catalysts higher in reactivity than most dispersed metal catalysts typically used in practice on both gravimetric and site bases. Kinetic trends reflect the stoichiometry of each hydrogenation reaction, as is also the case for their reverse directions (dehydrogenation), consistent with sites that remain essentially bare during catalysis. DFT-derived energies and free energies indicate that hydrogenation involves heterolytic channels and anionic organic intermediates that react with bound $H^{\delta+}$ species in the rate-limiting step. Such inferences lead to DFT-derived barriers that are negative and in agreement with measured values for acyclic alkenes (e.g., −58 vs −48 ± 2 kJ $mol^{-1}$ for $C_3H_6$). Reaction coordinates determined by DFT also show that the interconversion between *n*-$C_3H_7^-/H^+$ and $C_3H_8$ (or $C_2H_4$ analogs) remains the only kinetically relevant step at a wide range of conditions and in both reaction directions (hydrogenation and dehydrogenation). Hydrogenation and dehydrogenation activation barriers differ by the overall reaction enthalpies for all reactants. Consequently, De Donder formalisms can be applied to accurately predict dehydrogenation rate constants for alkanes, cycloalkanes, and arene side chains from hydrogenation rates and thermodynamic data for each reaction.

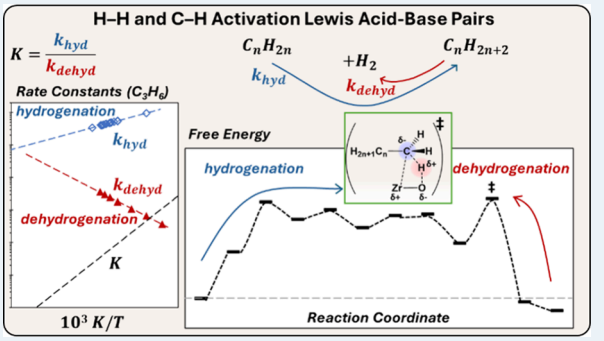


**KEYWORDS:** *hydrogenation, earth-abundant catalyst, Lewis acid–base pairs, $ZrO_2$, reaction mechanism, site titration, DFT (density functional theory), De Donder*



## 1. INTRODUCTION

Catalytic hydrogenations of unsaturated hydrocarbons provide routes for the manufacture of organic energy carriers and chemical intermediates, as well as strategies for stabilizing and upgrading polyunsaturated foodstuffs, pharmaceuticals, agrochemicals, and polymers.[1] These reactions are typically mediated by dispersed Pt, Pd, Rh, and Ni nanoparticles, which enable practical rates and selectivities but also require scarce elements that exhibit strong sensitivity to organosulfur and organonitrogen feed impurities.[2] The scarcity and cost of these elements and their sensitivity to poisons have motivated a persistent search for less costly and more sustainable alternatives.[3]

The pursuit of solids based on earth-abundant elements led to this study of $ZrO_2$-based materials with surface Lewis acid–base (LAB) Zr–O site pairs as catalysts for these reactions. The most competent Zr–O pairs are typically covered by strongly bound $H_2O$ and $CO_2$ during synthesis and subsequent exposure to ambient air,[4−6] but chemical treatments that react with such titrants without stranding organic residues are able to uncover uniquely active LAB pairs without thermal treatments at temperatures that sinter and anneal oxide crystallites. Such effects of thermal treatments are evident for butadiene hydrogenation reactions using $ZrO_2$ catalysts, for which higher thermal treatments first led to an increase in hydrogenation rates with increasing treatment temperature, but ultimately to much lower rates after treatments above 873

Received: May 22, 2025
Revised: June 29, 2025
Accepted: July 1, 2025
Published: July 11, 2025

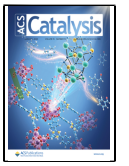




https://doi.org/10.1021/acscatal.5c03523
ACS Catal. 2025, 15, 12610–12626

K, a likely consequence of a significant loss of surface area.[7,8] Dimethyl ether (DME) was shown to be especially effective as a chemical treatment agent in uncovering such sites at mild conditions that prevent catalyst degradation.[4−6]

This study reports the high turnover rates for hydrogenation of alkenes, cycloalkenes, and unsaturated pendant chains in arenes on LAB pairs exposed at monoclinic zirconia ($m$-$ZrO_2$) surfaces by chemical treatments.[7,9−14] DME treatments at 723 K led to 30- to 100-fold increases in C=C bond hydrogenation rates compared with the rates observed on samples treated in He at the same temperature as a desorptive treatment. Such rates can be preserved during catalysis only by the strict removal of $H_2O$ and $CO_2$ titrants (or any of their precursors; e.g., $O_2$) from inlet streams because such molecules reverse the effects of chemical treatments during hydrogenation reactions. The resulting gravimetric $C_3H_6$ hydrogenation rates on DME-treated $m$-$ZrO_2$ are comparable to those reported on dispersed noble metal nanoparticles. These remarkably active LAB site pairs represent a small fraction of all Zr−O site pairs exposed at $m$-$ZrO_2$ surfaces, as shown by site counts derived from their purposeful titration with $H_2O$ pulses during catalysis. Such sites expose low-coordination Zr and O centers, which enable strong concerted interactions of the C and H atoms with the Zr and O atoms at LAB pairs, respectively, stabilizing the kinetically relevant C−H formation transition state (TS) for these reactions.

The stability conferred by strictly anhydrous and anaerobic conditions and the uncovering of low-coordination sites by chemical treatments allows precise measurements of kinetic trends and their unequivocal mechanistic interpretation in terms of the H−H activation and H-addition elementary steps that mediate hydrogenation turnovers. These steps include heterolytic H−H cleavage at LAB site pairs with anionic and cationic H species bound at the Zr and O atoms, respectively. The anionic H species react with a bound alkene, cycloalkene, or unsaturated arene side chain to form bound anionic alkyls, to which cationic H species eventually add to form the hydrogenated products in the sole kinetically relevant step for $C_2H_4$, $C_3H_6$, cyclopentene, and styrene hydrogenation. DFT-derived energies of bound intermediates and transition states confirmed the mechanistic interpretation of these kinetic trends in terms of these elementary steps and their respective reversibility and kinetic relevance.

The rates of the reverse dehydrogenation reactions (of $C_2H_6$, $C_3H_8$, cyclopentane, and ethylbenzene) are enhanced to a similar extent as for their hydrogenation counterparts by the uncovering of the same Zr−O pairs through chemical treatments. Both hydrogenation and the reverse dehydrogenation reactions occur on sites that remain essentially bare during catalysis. They proceed via the exact microscopic reverse elementary steps that mediate hydrogenation turnovers on the same LAB site pairs; the reactions share in the two directions the same kinetically relevant C−H formation/cleavage event that interconverts anionic alkyls and saturated hydrocarbon. The rates of each reaction depend on the stoichiometry of the kinetically relevant TS and obey the law of mass action in both directions, as expected from catalysis on sites that remain largely unoccupied during catalysis. Such kinetic trends allow the use of De Donder relations at the kinetically relevant elementary step, even far from the equilibrium conditions required for the rigorous enforcement of microscopic reversibility principles. Measured activation energies for hydrogenation and dehydrogenation differ by the enthalpy of each gas-phase interconversion reaction and act as compelling evidence for the conceptual and mechanistic links between hydrogenation and dehydrogenation catalytic sequences and for the rigorous thermodynamic origins of the ratio of their respective rate constants. These thermodynamic relations enable accurate predictions of rates in one direction from those measured in the reverse direction. The conclusions and guidance from these mechanistic and thermodynamic treatments are expected to broadly influence the design and use of heterolytic cleavage channels for the activation of X−H bonds (X = H, C, O) at low-coordination LAB pairs at oxides of diverse compositions.

## 2. METHODS

**2.1. Catalyst Synthesis Procedures.** $m$-$ZrO_2$ samples were prepared by first mixing separate solutions of $ZrO(NO_3)_2{\cdot}xH_2O$ (Sigma-Aldrich, 99%, 12.7 g) and $CO(NH_2)_2$ (urea; Sigma-Aldrich, 99.5%; 21.6 g) each in 30 $cm^3$ $H_2O$ (18.2 MΩ-cm) at 323 K.[15] The combined mixture of solutions was sealed within Teflon-lined autoclaves and held at 393 K for 20 h before cooling to ambient temperature and then isolating the solids by centrifugation. The solids were rinsed three times using 50 $cm^3$ $H_2O$ with intervening centrifugation and then treated in ambient air at 393 K for 12 h to give $ZrO_{2-x}(OH)_{2x}{\cdot}yH_2O$ precursors. These were subsequently heated in flowing dry air (ultra Zero, Praxair, 1.6 $cm^3\ g^{-1}\ s^{-1}$) to temperatures between 570 and 1108 K (at 0.17 K $s^{-1}$); and held for 5 h. The surface area of these powders was determined (after treatment in dynamic vacuum at 473 K for 4 h) by $N_2$ uptakes at its normal boiling point (Micromeritics 3Flex analyzer) using the Brunauer-Emmett-Teller formalism (air treatment temperature and surface area; 573 K: 190 $m^2\ g^{-1}$; 723 K: 130 $m^2\ g^{-1}$; 853 K: 106 $m^2\ g^{-1}$; 1023 K: 58 $m^2\ g^{-1}$; 1108 K: 33 $m^2\ g^{-1}$). $ZrO_2$ crystal sizes were determined from surface areas and confirmed by line breadth analysis of X-ray diffractograms (Rigaku Miniflex, Cu−K$\alpha$ radiation, 20−80° with a step scan of 0.01° $s^{-1}$) using the Scherrer equation;[4] diffractograms also showed that $m$-$ZrO_2$ was the predominant crystal phase in these materials.

**2.2. Chemical Treatment Procedures and Alkane Dehydrogenation Rate Measurements.** $m$-$ZrO_2$ powders (sieved to 180−250 $\mu$m aggregates) were mixed with inert quartz diluent (Sigma-Aldrich, previously washed with 1 M $HNO_3$; from stock Nitric Acid, ACS Plus; A200C-212, Lot 233861 and treated in flowing dry air at 1073 K for 8 h; 180−250 $\mu$m) to mass ratios of 1:50 (typically 0.02−0.1 g $ZrO_2$). The $ZrO_2$-quartz mixtures were held by quartz wool within a U-shaped quartz tubular reactor (internal diameter: 1 cm) or straight reactor (inner diameter: 7 mm). The reactor was heated resistively (3210, Applied Test Systems); the temperature was controlled electronically (Watlow 96) and measured by a K-type thermocouple in contact with the outer reactor wall at the catalyst bed axial midpoint. The samples were treated in flowing He (Praxair, 99.999%; 40−100 $cm^3\ g^{-1}\ s^{-1}$) by heating to 723 K (at 0.33 K $s^{-1}$) and holding for 1 h before DME or He treatments and reaction rate measurements. Bound titrants were removed by contact with dimethyl ether (DME; 1.5 kPa; Praxair, 5.0% DME, 5.1% Ar in He; 40 $cm^3\ g^{-1}\ s^{-1}$) for 0.25 h at 723 K and subsequent exposure to flowing He (40 $cm^3\ g^{-1}\ s^{-1}$) for 0.42 h. $O_2$ treatments (Praxair, 99.99%, 5% $O_2$ in He; 40 $cm^3\ g^{-1}\ s^{-1}$ for 0.5 h at 723 K) were optionally used to remove any carbonaceous deposits that may have formed after extended use.


https://doi.org/10.1021/acscatal.5c03523
ACS Catal. 2025, 15, 12610−12626

Rates and selectivities were measured by flowing mixtures of He and $H_2$ (Praxair, 99.999%) with $C_2H_6$ (Praxair, 50% in Ar, 99.999%), $C_2H_4$ (Praxair, 91% in Ar), $C_3H_8$ (Praxair, 20−50% in Ar, 99.999%), or $C_3H_6$ (49.9% in He, 99.999%) through the catalyst bed. Impurities were removed from reactants or reactant mixtures by passage through a $H_2O/O_2$ scrubber (Agilent 5182−9401, 5 ppb). Liquid hydrocarbons consisted of ethylbenzene (Sigma-Aldrich, 99.5+%), cyclopentane (Thermo Scientific Chemicals, HPLC grade), cyclopentene (Alfa Aesar, ≥98%), and styrene (Sigma-Aldrich, 99.5+%, stabilized with 4-*tert*-butylcatechol). Liquids were deaerated by He flow for 0.5 h at 293 K and ethylbenzene and cyclopentane were additionally purified by refluxing over freshly calcined molecular sieves (CBV720; treated at 773 K in zero-air for 12 h). Cyclopentane and ethylbenzene liquids were then contacted with molecular sieves (4A; freshly treated at 723 K in zero-air for 12 h) before placing them within a stainless-steel vessel connected to the reactor influent stream through a fine metering valve. These reactants were introduced by heating the vessel and the contained liquid to a temperature 5−10 K above their respective boiling points and adjusting the connecting needle valve to deliver the intended partial pressures, which were confirmed chromatographically. Alternatively, styrene and cyclopentene were introduced via a syringe pump. Gaseous alkenes and all reactants introduced by vaporization were combined with the $H_2$/He stream after the scrubber, a requirement imposed by their retention or hydrogenation by the absorbent present within the scrubber.

Reactant and product concentrations were measured by online gas chromatography (Agilent 6890A GC) using flame ionization detection (FID) and a capillary column (Agilent; HP-1 or GS-GasPro). Rates were measured at different alkene, alkane, and $H_2$ pressures (1−100 kPa); they are reported as molar rates of formation of the respective product per mass (gravimetric), per surface area (areal) or per active site (turnover rates, measured by site titration using $H_2O$; see Section 2.3). Forward rates ($r_f$) were determined by correcting measured rates ($r_{net}$) for approach to equilibrium ($\eta$), calculated from the axial mean of the partial pressures of reactants and products and the equilibrium constant ($K_{eq}$) of the respective reactions using eqs 1 and 2:

$$r_f = \frac{r_{net}}{1 - \eta} \tag{1}$$

$$\eta = \frac{\prod_j P_j}{\prod_i P_i} K_{eq}^{-1} \tag{2}$$

where $P$ is the mean reactor pressure of products ($j$) or reactants ($i$) (in units of bars). All selectivities are reported on a carbon basis and contributions from homogeneous reactions (typically <0.2% of the catalytic rates) were subtracted from all reported rates and selectivities.

The presence of residual titrants in inlet streams after purification leads to the gradual deactivation of chemically cleaned catalysts through a first-order process that can be fully reversed by chemical treatments with DME. Reported rates are corrected for deactivation by extrapolating forward rates ($r_{f,t}$) to the initial time of contact with reactants by using such first-order deactivation models:

$$r_{f,t} = r_0 e^{-k_d t} \tag{3}$$

where $r_{f,t}$ is the forward rate at time $t$, $r_0$ is the reaction rate at the initial time of reactant contact for the given condition, and $k_d$ is the deactivation rate constant that reflects the rate of arrival of the residual stoichiometric titrants in the inlet stream (deactivation rates correspond to residual titrant levels of about 100 ppb, estimated from deactivation rates and the number of active sites determined by the intentional titration of sites using $H_2O$ pulses).

**2.3. Measurements of the Number of Active Sites by $H_2O$ Titration Protocols during Catalysis.** The strong binding of $H_2O$ at the most competent LAB sites at *m*-$ZrO_2$ surfaces was exploited to determine the number of such sites during catalytic reactions after a given chemical treatment. $H_2O$ pulses (0.29 $\mu$mol) were injected by preparing a stream of He (0.167−0.833 $cm^3\ s^{-1}$) that was saturated with $H_2O$ liquid water at 273 K and injecting this mixture as aliquots held in the sample loop of a six-port switching valve (423 K, 1 $cm^3$; VICI) into the reactant stream (0.833 $cm^3\ g^{-1}\ s^{-1}$). Effluent concentrations were measured using the chromatographic protocols described in Section 2.2 and from fragmentation patterns in a mass spectrometer (MKS Cirrus 3) using reported deconvolution methods.[16] These protocols were used to determine the number of active sites from the number of $H_2O$ molecules required to fully suppress the reaction rates.

**2.4. Computational Methods.** The Vienna ab initio simulation package (VASP 5.4.4[17]) was used to carry out density functional theory (DFT) estimates of enthalpies and free energies of reactants, products, intermediates, and transition states for $C_2H_4$ and $C_3H_6$ hydrogenation reactions on a model *m*-$ZrO_2$(−111) surface at the Zr−O pair that binds $H_2O$ most strongly (described below). These computations used the generalized gradient approximation (GGA) as prescribed in Perdew−Burke−Ernzerhof (PBE) methods with[18] Grimme's dispersion corrections (D3)[19] at each energy minimization step to account for van der Waals interactions and dipole corrections to eliminate long-range interactions among periodic images. Valence and core electrons were described using projector-augmented wave pseudopotentials with plane-wave basis sets restricted by a cutoff of 450 eV.[20] The Brillouin zone was sampled with a 3 × 3 × 1 Monkhorst−Pack[21] k-point grid. Energies converged with a criterion of $10^{-6}$ eV in self-consistent steps and forces were converged to 0.05 eV $Å^{-1}$. Nudged elastic band (NEB) methods[22] were used to isolate transition states (TS) from typically 10−12 images, and the saddle point was refined with the climbing image method[23,24] before further refinement of TS structures using the Henkelman Dimer method.[25] Reported energies are referenced to the relevant structures of a bare surface, gaseous alkene, and $H_2$.

A 9 × 9 × 6 Monkhorst Pack k-point grid[26] was used to generate the slab model of *m*-$ZrO_2$(−111)[27,28] surface (the lowest surface energy facet[29−33]) using optimized lattice constants (a = 0.522 nm, b = 0.528 nm, c = 0.539 nm; within 2% of those reported in the literature).[34−40] A [2 × 2]-supercell was used to construct the slab model with four layers (Zr basis in the *c*-axis direction) and a 1.65 nm vacuum layer among the slabs. The bottom two layers of $ZrO_2$ slabs were frozen at their bulk crystallographic positions during all energy optimizations of bound species in order to preserve the integrity of the subsurface crystal structure. The top view[41] of the [2 × 2] *m*-$ZrO_2$ supercell surface, is shown in Figure 1. There are four coordinatively distinct Zr-atoms; $Zr_1$, $Zr_2$, and $Zr_3$ centers are six-coordinate and $Zr_4$ is seven-coordinate.


https://doi.org/10.1021/acscatal.5c03523
ACS Catal. 2025, 15, 12610−12626

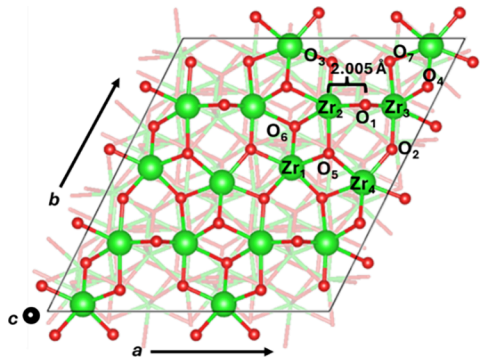


**Figure 1.** Depiction of the model $m$-$ZrO_2$(−111) surface, where surface atoms are represented by ball and stick and subsurface atoms by wireframe.

Computations were carried out on $Zr_2$ and the two-coordinate $O_1$ atom along the $a$-axis; a Zr−O bond distance of 2.0 Å, because $H_2O$ is known to bind most strongly on this Zr−O site pair (−132 kJ $mol^{-1}$) among all pairs surveyed on the surface (−30 to −132 kJ $mol^{-1}$) and hydrogenation active sites are readily titrated by $H_2O$.

Energies, enthalpies, entropies, and free energies were computed from DFT electronic energies and vibrational frequency assessments, as described in detail in Section S.1; Supporting Information. Briefly, vibrational frequencies for all structures were estimated with the harmonic oscillator approximation using atomic displacements of ± 0.0015 nm. Enthalpies were estimated from zero-point vibrational energies ($E_{ZPV}$) and vibrational frequencies.[42] Entropies were estimated from DFT-derived vibrational frequencies using statistical mechanics formalisms.[42] The inaccuracies of harmonic oscillator models in describing low-frequency modes lead to large entropy overestimates for bound species;[43] consequently, contributions to entropies from low-frequency modes (<90 $cm^{-1}$) were replaced with a fraction of the corresponding rotational and translational entropies of the gaseous analogs of bound species. A fraction of 0.7 is commonly applied, reflecting the loss of one degree of translational freedom in the axis normal to the surface when the molecule is bound to the surface. The maximum number of low modes ($\#_{low\text{-}modes}$) that can be excluded is six for nonlinear and five for linear molecules, corresponding to the number of translational and rotational degrees of freedom for each molecule type. As such, low-frequency modes were replaced with either (0.7 × ($\#_{low\text{-}modes}$)/6) or (0.7 × ($\#_{low\text{-}modes}$)/5) of the rotational and translational energy of the gas phase, depending on the adsorbate molecule.[44−46]

Free energies ($G$) were calculated using

$$G = E_0 + E_{ZPV} + H_{vib} + H_{trans+rot} - T\left(S_{vib} + 0.7\frac{\#_{low-modes}}{5 \text{ or } 6}S_{trans+rot}\right) \quad (4)$$

where $E_0$ is the DFT-derived electronic energy and the vibrational (vib), translational (trans), and rotational (rot) contributions to enthalpy and entropy are indicated by the respective subscripts.[47] All reported enthalpies, free energies, and entropies are reported at a temperature of 723 K.

## 3. RESULTS AND DISCUSSION

**3.1. Rates and Kinetic Trends for C=C Bond Hydrogenation.** *3.1.1. Hydrogenation of Linear Alkenes ($C_2H_4$ and $C_3H_6$) and the Kinetic Competence of m-$ZrO_2$ in Hydrogenation Reactions.* $C_2H_4$ hydrogenation rates (per mass; 9.2 kPa $C_2H_4$, 5.6 kPa $H_2$; 723 K) upon initial contact of reactants with $m$-$ZrO_2$ catalysts are about 80-fold higher for samples that are chemically treated (723 K) with DME ($r_i$: 230 mol $kg^{-1}$ $h^{-1}$) than when the same sample is treated in He at 723 K (2.8 mol $kg^{-1}$ $h^{-1}$; Table 1). DME treatments led to similar rate enhancements for the reverse reaction ($C_2H_6$ dehydrogenation; 15 kPa $C_2H_6$; 773 K), for which rates increased from 0.19 mol $kg^{-1}$ $h^{-1}$ after treatment in He at 723 K to 14 mol $kg^{-1}$ $h^{-1}$ after DME treatment at 723 K (Table 1). The similar rate enhancements for hydrogenation and dehydrogenation reactions indicate that the same active sites, specifically those from which DME removes bound $H_2O$,[7,9−14] are responsible for the rates measured in both directions. These results also show that DME treatments uncover LAB site pairs at $m$-$ZrO_2$ surfaces and that such sites are uniquely competent at stabilizing the TS structure(s) that mediate hydrogenation and dehydrogenation turnovers at $m$-$ZrO_2$ surfaces.[5] These DME-treated $m$-$ZrO_2$ catalysts are used next to measure rates and kinetic trends for the hydrogenation of several unsaturated molecules and to assess the identity, reversibility, and kinetic relevance of the requisite elementary steps along the reaction coordinate at the most active LAB site pairs on the $m$-$ZrO_2$ surfaces.

$C_2H_4$ hydrogenation rates at different $C_2H_4$ (2−13 kPa) and $H_2$ (1−9 kPa) pressures were measured on DME-treated $m$-$ZrO_2$ at differential conditions ($C_2H_4$ fractional conversions <0.1) and conditions far from equilibrium ($\eta$ < 0.1; eq 2). $C_2H_4$ hydrogenation rates upon initial contact of reactants with DME-treated $m$-$ZrO_2$ are shown in Figure 2a. $C_2H_4$ hydrogenation rates ($r_h$) were strictly proportional to the pressures of $C_2H_4$ and $H_2$:

**Table 1. Gravimetric Rates of Unsaturated Hydrocarbon Hydrogenation and Corresponding Reverse Dehydrogenation Reactions on $m$-$ZrO_2$ Treated with He or DME at 723 K**

| | hydrogenation rates (mol·$kg^{-1}$·$h^{-1}$) | | | corresponding dehydrogenation rates (mol·$kg^{-1}$·$h^{-1}$) | | |
|---|---|---|---|---|---|---|
| reactant | He-treated | DME-treated | enhancement factor[e] | He-treated | DME-treated | enhancement factor[e] |
| $C_2H_4$[a] | 2.8 | 230 | 82 | 0.19 | 14 | 74 |
| $C_3H_6$[b] | 14 | 1360 | 97 | 0.30 | 36 | 120 |
| cyclopentene[c] | 0.2 | 5.4 | 27 | 0.005 | 0.19 | 38 |
| styrene[d] | 0.3 | 15 | 50 | 0.015 | 0.94 | 62 |

[a]9.2 kPa $C_2H_4$, 5.6 kPa $H_2$ at 723 K for hydrogenation and 15 kPa $C_2H_6$, 5.1 kPa $H_2$ at 773 K for dehydrogenation. [b]13.7 kPa $C_3H_6$, 12.3 kPa $H_2$ at 723 K for hydrogenation and 15 kPa $C_3H_8$ 5.1 kPa $H_2$ at 723 K for dehydrogenation. [c]1.6 kPa $C_5H_8$, 100 kPa $H_2$ at 598 K for hydrogenation and 1.6 kPa $C_5H_{10}$, 12 kPa $H_2$, 723 K for dehydrogenation. [d]1.9 kPa $C_8H_8$, 12 kPa $H_2$ at 573 K for hydrogenation and 1.8 kPa $C_8H_{10}$ 12 kPa $H_2$, 723 K for dehydrogenation. [e]Enhancement factors reflect the ratio of rates on samples treated with DME and He at 723 K.



https://doi.org/10.1021/acscatal.5c03523
ACS Catal. 2025, 15, 12610−12626

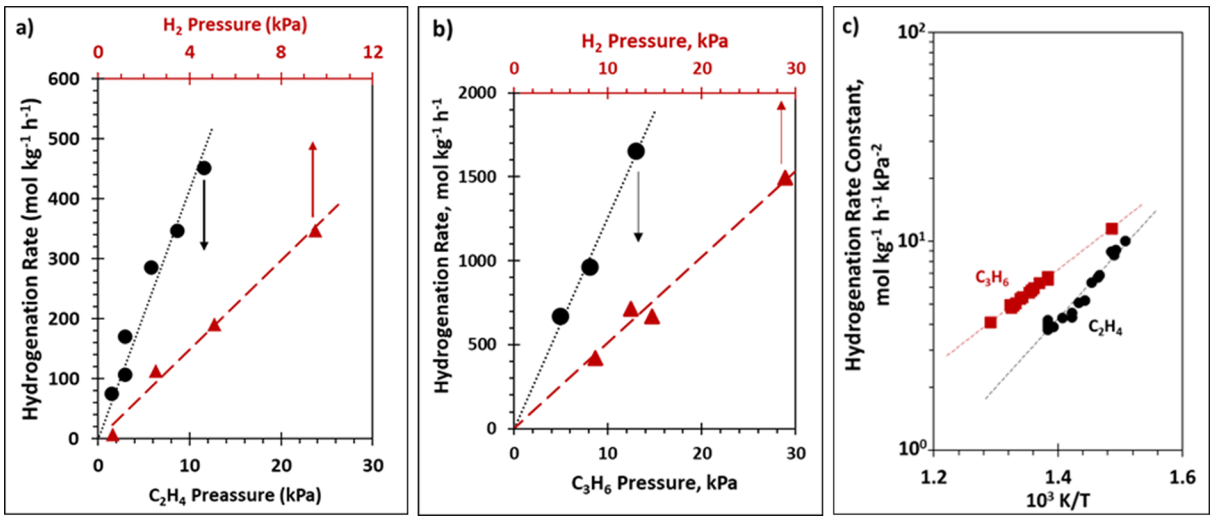


**Figure 2.** (a) Gravimetric rates of $C_2H_4$ hydrogenation on DME-treated *m*-$ZrO_2$ at 723 K as a function of $C_2H_4$ pressure (black circles, ●●●; at 9.5 kPa $H_2$) and $H_2$ pressure (red triangles, - - -; at 8.6 kPa $C_2H_4$). (b) Gravimetric rates of $C_3H_6$ hydrogenation on DME-treated *m*-$ZrO_2$ at 723 K as a function of $C_3H_6$ pressures (black circles, ●●●; at 14.7 kPa $H_2$) and $H_2$ pressure (red triangles, - - -; at 5 kPa $C_3H_6$). (C) Second-order rate constants for $C_2H_4$ (black circles) and $C_3H_6$ (red squares) hydrogenation as a function of the reciprocal absolute temperature.

$$r_h = k_h \times P_{C_nH_m} \times P_{H_2} \quad (5)$$

with $k_h$ as the second-order rate parameter for each given unsaturated hydrocarbon, $C_nH_m$. These kinetic trends reflect the overall stoichiometry of the hydrogenation reaction and thus the law of mass action kinetics, as previously observed for the reverse reaction (ethane dehydrogenation) on *m*-$ZrO_2$ catalysts, whose rates were also enhanced (74-fold) by DME treatments.[6]

Gravimetric $C_3H_6$ hydrogenation rates (per mass; 13.7 kPa $C_3H_6$, 12.3 kPa $H_2$; 723 K) on He-treated *m*-$ZrO_2$ were 14 mol $kg^{-1}$ $h^{-1}$ after treatment in He at 723 K and 1360 mol $kg^{-1}$ $h^{-1}$ after DME treatment at the same temperature. This nearly 100-fold rate enhancement conferred by the DME-mediated removal of strongly bound titrants is similar to that found for $C_2H_4$ hydrogenation. $C_3H_8$ dehydrogenation rates were also enhanced by DME treatments by a similar factor (~120; from 0.30 to 36 mol $kg^{-1}$ $h^{-1}$). $C_3H_6$ hydrogenation rates were proportional to $C_3H_6$ and $H_2$ pressures (Figure 2b; 5−13 kPa $C_3H_6$; 8−30 kPa $H_2$), consistent with the hydrogenation reaction stoichiometry and with the kinetic trends observed for $C_2H_4$ hydrogenation; these rates are accurately described by the functional form of eq 5. Rates of the reverse reaction ($C_3H_8$ dehydrogenation) were proportional to $C_3H_8$ pressures and consistent with the stoichiometry of the dehydrogenation reaction and with the law of mass action kinetics. Hydrogenation and dehydrogenation rates for both $C_2$ and $C_3$ (alkene/alkane) reactants show kinetic trends that reflect the respective stoichiometry of the reaction in both directions, and the proportional relations of rates with reactant pressures reflect the prevalence of bare Zr−O pairs during steady-state catalysis at all conditions.

$C_2H_4$ and $C_3H_6$ hydrogenation rates decreased with time, in a manner described by first-order deactivation formalisms. $C_2H_4$ hydrogenation rates (after initial DME treatment) decreased from about 200 to about 100 mol $kg^{-1}$ $h^{-1}$ over 1.2 ks (first-order deactivation rate constant, $k_d$: 0.7 $ks^{-1}$) when $C_2H_4$/He and $H_2$ streams were passed through separate $O_2$/$H_2O$ scrubbers (Figure S1; Supporting Information). Subsequent DME treatments fully restored initial $C_2H_4$ hydrogenation rates, while He treatments cannot. Subjecting the catalyst to reaction mixtures that have not passed through scrubbers results in an increased deactivation rate ($k_d$: 6.8 $ks^{-1}$), but even under such conditions, DME treatments were sufficient to restore the initial rates. Neither He nor $O_2$ treatments at 723 K for 3.6 ks restored the initial rates after deactivation, indicating that organic residues are not responsible for the observed loss of reactivity and that DME treatments react with strongly bound species. DME removes bound $H_2O$ titrants via hydrolysis reactions at modest temperatures (500−723 K),[48] as shown by the formation of $CH_3OH$ during such treatments by online mass spectrometry. The congruence of evidence supporting site deactivation by trace water impurities in the inlet stream justifies the rate corrections for deactivation described in Section 2.3

The hydrogenation rate constants for acyclic alkenes were determined from measured rates at different temperatures (573−773 K) by using fast temperature decrease protocols and correcting for any intervening deactivation (Figure 2c; $C_2H_4$ and $C_3H_6$ hydrogenation). These hydrogenation rate constants show the expected Arrhenius-type temperature dependence but decrease with increasing temperature, instead of the rate increase with temperature typical of most chemical reactions. This reflects a kinetically relevant TS for hydrogenation that is lower in enthalpy than the reactants (unsaturated hydrocarbon molecule, $H_2$, and a bare LAB site pair), leading to these negative apparent activation energies (−52 ± 9 and −48 ± 2 kJ $mol^{-1}$ for $C_2H_4$ and $C_3H_6$, respectively). The functional form of the rate expression (eq 5) requires that the kinetically relevant TS contains an ensemble of atoms that include the two H atoms in $H_2$ and all of the C atoms and H atoms in each alkene and that Zr−O pairs remain essentially uncovered by bound species at all reaction conditions; similar conclusions were reached for the reverse reaction ($C_2H_6$ and $C_3H_8$ dehydrogenation), for which activation barriers were positive, but which also occurred on bare surfaces at rates limited by a step involving a TS with the stoichiometric composition of an alkane molecule.[6] The functional form of the respective rate equations for hydrogenation and dehydrogenation reactions and the opposite temperature trends for their rate constants


https://doi.org/10.1021/acscatal.5c03523
ACS Catal. 2025, 15, 12610−12626

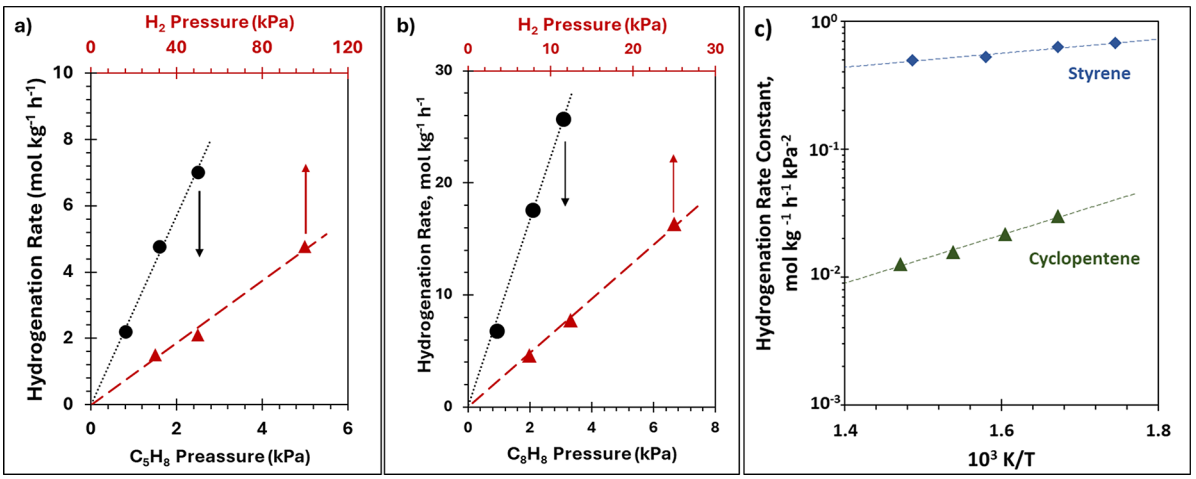


**Figure 3.** (a) Gravimetric rates of $C_5H_8$ hydrogenation on DME-treated *m*-$ZrO_2$ at 598 K as a function of $C_5H_8$ pressure (black circles, ●●●; at 100 kPa $H_2$) and $H_2$ pressure (red triangles, - - -; at 1.6 kPa $C_5H_8$). (b) Gravimetric rates of $C_8H_8$ hydrogenation on DME-treated *m*-$ZrO_2$ at 573 K as a function of $C_8H_8$ pressures (black circles, ●●●; at 12 kPa $H_2$) and $H_2$ pressure (red triangles, - - -; at 1.9 kPa $C_8H_8$). (C) Second-order rate constants for $C_5H_8$ (green triangles) and $C_8H_8$ (blue diamonds) hydrogenation as a function of the reciprocal absolute temperature.

suggest that the ratio of the two rate constants may simply reflect the thermodynamics of the overall reaction, for which enthalpies and entropies are known from tabulated data for the gaseous species involved; these expectations and the involvement of the same TS in both directions are confirmed in Sections 3.3 and 3.4 by DFT assessments of the forward and reverse reaction pathways, which shed light on the origins of such a link between the kinetics and the thermodynamics of these reactions.

*3.1.2. Hydrogenation of C═C Bonds in Cyclic Alkenes (Cyclopentene) and in Pendant Alkene Chains in Arenes (Styrene).* The reactivity of Zr−O site pairs for the hydrogenation of C=C bonds in cycloalkenes and vinyl pendant chains in arenes was examined for reactions of cyclopentene ($C_5H_8$) and styrene ($C_8H_8$) with $H_2$. Cyclopentene hydrogenation (1 to 3 kPa $C_5H_8$; 50−100 kPa $H_2$; 598 K) on DME-treated *m*-$ZrO_2$ forms exclusively cyclopentane without detectable ring-opening reactions. Likewise, styrene (1−7 kPa) reactions with $H_2$ (5−25 kPa) on DME-treated *m*-$ZrO_2$ (573−673 K) forms only ethylbenzene, without any evidence for C−C cleavage or ring hydrogenation, reflecting, at least in part, unfavorable thermodynamics. These findings underscore the highly selective hydrogenation of vinyl C═C double bonds relative to the hydrogenation of aromatic rings and highlight the unique capability of Zr−O site pairs to enable targeted hydrogenations under mild conditions.

Cyclopentene hydrogenation rates on *m*-$ZrO_2$ (1.6 kPa cyclopentene, 100 kPa $H_2$, 598 K; Table 1) increased from 0.2 to 5.4 mol $kg^{-1}$ $h^{-1}$ by treatment with DME at 723 K compared to treatment in He at 723 K, a 27-fold enhancement. The reverse cyclopentane dehydrogenation reaction shows a 38-fold rate enhancement upon DME treatment (cf. He treatment; 723 K; Table 1) and forms only cyclopentene. Cyclopentadiene was not detected, as expected from low cyclopentene pressures in the catalyst bed, which would lead to cyclopentadiene pressures below detection limits (0.2 Pa $C_5H_8$; assuming similar dehydrogenation rate constants for each hydrocarbon).

The rates of styrene hydrogenation to ethylbenzene (1.9 kPa styrene, 12 kPa $H_2$, 573 K, Table 1) increased 50-fold (0.3 to 15 mol $kg^{-1}$ $h^{-1}$) after treatment of *m*-$ZrO_2$ with DME at 723 K. The reverse ethylbenzene dehydrogenation reaction (to styrene) increased 62-fold by DME treatment (Table 1). Lower rate enhancements for both hydrogenation and reverse dehydrogenation reactions for cyclopentene/cyclopentane and styrene/ethylbenzene pairs compared to linear alkene/alkane transformations may reflect inhomogeneities of active site sampling by the kinetically relevant TS for each substrate class. The broad $H_2O$ desorption profile observed during thermal treatment in He (303−1108 K) of *m*-$ZrO_2$ samples initially exposed to ambient moisture indicates a range of $H_2O$ binding energies, and presumably a range of TS stability. Relations between the TS for $H_2O$ and hydrocarbon binding depend on the lateness for each specific reactant, but nonequivalent binding indicates that Zr−O sites differ in their competence for adsorbate binding (described in Section 3.2). The larger molecules would apparently benefit less from the broader distribution of sites made available by DME treatment compared to the short, acyclic alkenes. Such assessments are outside the scope of this work but will be addressed by theoretical treatments in future work.

Cyclopentene and styrene hydrogenation rates on DME-treated *m*-$ZrO_2$ are proportional to the hydrocarbon (0.4−4 kPa) and $H_2$ (8−100 kPa) pressures (Figure 3a,b), as also observed for ethene and propene hydrogenation (Figure 2). These kinetic trends reflect the respective reaction stoichiometries and obey the functional form of eq 5. They indicate that the kinetically relevant TS contains one molecule of the unsaturated substrate and two H atoms and that Zr−O site pairs remain essentially bare during these hydrogenation reactions. Second-order kinetic constants for hydrogenation reactions exhibit an Arrhenius-type temperature dependence over 573−673 K (Figure 3c) with the activation energies of −36 ± 5 and −10 ± 3 kJ·$mol^{-1}$ for cyclopentene and styrene hydrogenation, respectively. These *inverse* effects of temperature indicate that the kinetically relevant TS has a lower enthalpy than the reactant state for both reactions, as also found in the case of ethene and propene hydrogenation (Figure 2c). The rates of their respective reverse dehydrogenation reactions are also proportional to reactant pressures (Figure S2; Supporting Information) and their rate constants increase with temperature, consistent with positive apparent


https://doi.org/10.1021/acscatal.5c03523
ACS Catal. 2025, 15, 12610−12626

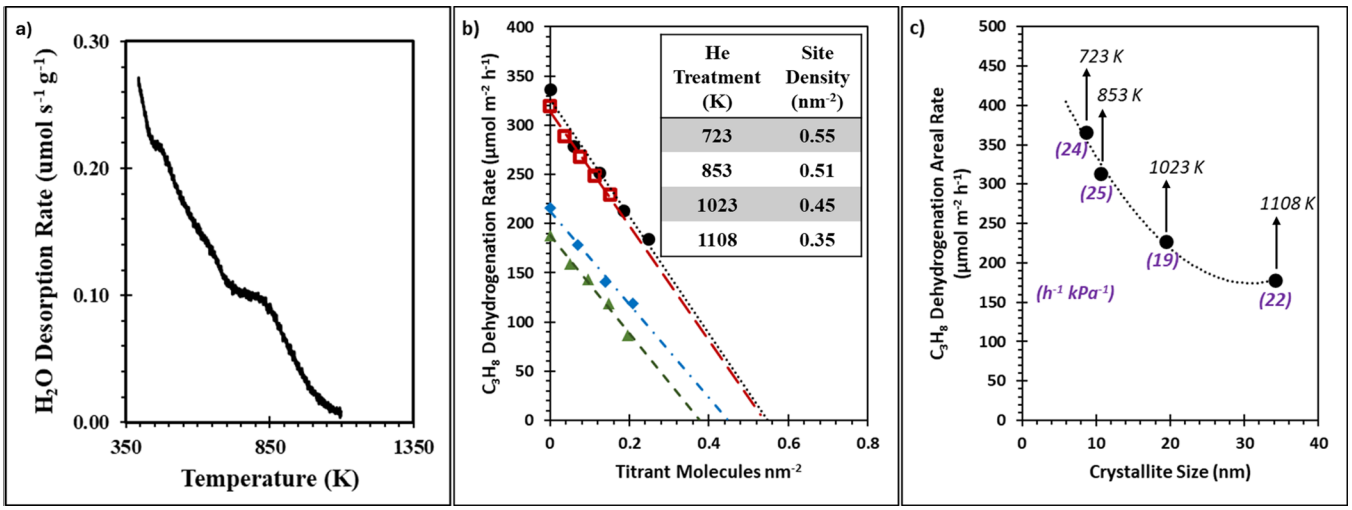


**Figure 4.** (a) $H_2O$ desorption rates from *m*-$ZrO_2$ in flowing He as the temperature increased from 303 to 1108 K (0.167 K $s^{-1}$). (b) Areal $C_3H_8$ dehydrogenation rates (15 kPa $C_3H_8$; 723 K) on DME-treated *m*-$ZrO_2$ [prior thermal treatments of 723 K (closed black circles, ●●●), 853 K (open red squares, – – ), 1023 K (closed blue diamonds, -●-), and 1108 K (closed green triangles, - -)] vs titrant molecules introduced during on-stream pulse titrations with 0.66 kPa $H_2O$. c) Areal $C_3H_8$ dehydrogenation rates and site-normalized rate constants (listed in parentheses) on DME-treated *m*-$ZrO_2$ as a function of crystallite size varied by He treatment temperature (arrows). Crystallite sizes were determined from surface areas determined from $N_2$ uptakes and the BET equation. Dashed lines and curves indicate visual trends.

activation energies. The thermodynamic links between each forward and reverse rate constant are confirmed by theoretical analyses in Sections 3.3 and 3.4, showing that reactions that proceed through the same TS in the forward and reverse directions on bare sites exhibit rates that are directly related by the thermodynamics of the overall reaction, even those far from equilibrium conditions.

The competence of the Zr−O pairs uncovered by chemical treatments for C═C bond hydrogenation in alkenes, cycloalkenes, and side chains in arenes is explored next explored (Section 3.2). Turnover rates are determined by normalizing rate constants by the number of active sites, required for rigorous benchmarking with reported materials and with theoretical assessments of the reaction pathway. The strong binding of $H_2O$ at active sites of *m*-$ZrO_2$ is used to determine active site densities by using $H_2O$ titration during catalysis. This analysis shows that active sites represent only a small fraction of Zr−O pairs at $ZrO_2$ surfaces and provides a metric for site reactivity used in comparison to literature-reported materials and also determines site-normalized rate constants, which are necessary for comparison to theoretical free energies computed by DFT in Sections 3.3.

**3.2. Determining the Number of Active Lewis Acid−Base Site Pairs at *m*-$ZrO_2$ Surfaces and Site Competence for $C_3H_6$ Hydrogenation.** Thermal treatment of *m*-$ZrO_2$ leads to the desorption of $H_2O$ from $ZrO_2$ surfaces, as shown by mass-spectrometric detection in the effluent stream during temperature ramping in He (303 to 1108 K; 0.167 K $s^{-1}$; after treatment at 303 K for 1 h; Figure 4a). The $H_2O$ evolution rate generally decreases over the reported temperature range. The broad desorption profile indicates a range of $H_2O$ binding strengths and suggests site heterogeneity among binding locations of $H_2O$. The area under this broad feature indicates that 1.9 $H_2O$ $nm^{-2}$ desorbed from *m*-$ZrO_2$ between 303 and 723 K, corresponding to weakly bound $H_2O$ that is readily removed by the He treatments at 723 K. The more strongly bound $H_2O$ molecules that desorb between 723 and 1108 K correspond to those present at *m*-$ZrO_2$ surfaces before contact with DME in the reactivity assessments; 0.62 $H_2O$ $nm^{-2}$ (130 $m^2$ $g^{-1}$ at 723 K basis) desorb above 723 K, serving as an estimate for the maximum $H_2O$ that occupies the active sites and prevents hydrogenation reactivity.

$H_2O$ and $CO_2$ (and the $O_2$ molecules that can form them during hydrogenation-dehydrogenation reactions) irreversibly titrate the LAB pairs responsible for hydrogenation-dehydrogenation reactions on *m*-$ZrO_2$. The purposeful introduction of known amounts of $H_2O$ into reactant streams allows for the counting of the sites responsible for these reactions from the number of titrant molecules required to fully suppress reaction rates. $C_3H_8$ dehydrogenation is used herein as the reaction probe, but the results also reflect the sites that are active for $C_3H_6$ hydrogenation. This is obvious from the similar rate enhancements conferred by DME treatments for a given reaction pair in both directions, the demonstration of these reactions occurring on the same model sites in both directions described in Section 3.3, and the thermodynamic links between the two reactions described in Section 3.4 that are possible only for reaction pairs that occur on the same sites. The $H_2O$ required to achieve full suppression of $C_3H_8$ dehydrogenation rates serves as an estimate of the number of sites blocked in the process of deactivating the catalyst.

Figure 4b shows areal propane dehydrogenation rates on *m*-$ZrO_2$ treated in He at different temperatures (723, 853, 1023, and 1108 K; 5 h), then treated with DME (723 K), and then exposed to a sequence of $H_2O$ pulses during $C_3H_8$ dehydrogenation (procedures in Section 2.3). Areal $C_3H_8$ dehydrogenation rates (15 kPa of $C_3H_8$) on *m*-$ZrO_2$ treated in He (723 K) and then in DME at 723 K (black circles; Figure 4b; 723 K; 130 $m^2$ $g^{-1}$) decreased linearly with the amount of $H_2O$ introduced, confirming the strong binding of $H_2O$ at the Zr−O site pairs responsible for measured rates. A linear extrapolation to zero rates (Figure 4a) gives the number of $H_2O$ molecules required to titrate all sites and thus the areal LAB site densities after samples were sintered and annealed to different extents by the preceding He treatments. Such areal densities decreased with increasing He treatment temperature


https://doi.org/10.1021/acscatal.5c03523
ACS Catal. 2025, 15, 12610−12626

Table 2. Reported $C_3H_6$ Hydrogenation Rates (per Mass and Site) and Reaction Conditions on Ni-, Rh-, Pt-, Pd-, Ir-, Co-, and Zn-Based Catalysts Compared to Expected Hydrogenation Rates for DME-treated *m*-$ZrO_2$ Using the Rate Relations Shown in Equation 5 and Figure 2c[d]

| | pressure (kPa) | | | | | | |
|---|---|---|---|---|---|---|---|
| catalyst | $C_3H_6$ | $H_2$ | temperature (K) | hydrogenation rates (mol $kg^{-1}$ $min^{-1}$) | turnover rates[b] ($s^{-1}$) | rates on *m*-$ZrO_2$ (mol $kg^{-1}$ $min^{-1}$)[a] | turnover rates on *m*-$ZrO_2$[c] ($s^{-1}$) |
| Ni(K)[53] | 11.1 | 11.1 | 313 | $4.6 \times 10^5$ | - | $2.0 \times 10^5$ | $2.9 \times 10^4$ |
| Rh/$TiO_2$-RNR[55−57] | 2 | 2 | 373 | 5.3 | - | 454 | 63 |
| 0.72% Pt/$TiO_2$[51,52] | 10 | 20 | 313 | 19 | 35 | $3.3 \times 10^5$ | $4.6 \times 10^4$ |
| Pd[49,50] | 10 | 90 | 308 | $1.7 \times 10^3$ | 62 | $1.9 \times 10^7$ | $2.8 \times 10^4$ |
| $[Ir_4(CO)_{12}]$/NaY[54,55] | 0.9 | 2.1 | 673 | $7.5 \times 10^{-2}$ | - | 0.36 | 0.05 |
| 12% Co-0.5%Re/$Al_2O_3$[58] | 25.7 | 154 | 393 | 1.7 | 0.07 | $2.1 \times 10^5$ | $2.9 \times 10^4$ |
| 3.9% Zn/$SiO_2$[59] | 0.6 | 3.4 | 473 | $3.3 \times 10^{-3}$ | - | 11 | 1.6 |

[a]Computed by extrapolation of the rate relations from Figure 2 to the experimental conditions listed for the literature catalysts. [b]From site counts measured by $H_2$ chemisorption and electron microscopy [c]From site densities measured with $H_2O$ titration during reaction; Section 3.2 [d]"-" indicates insufficient information reported to determine.

(Figure 4b) and are 0.55 $nm^{-2}$ for DME-treated *m*-$ZrO_2$ that was initially treated in He 723 K. This site density is similar to the number of bound $H_2O$ molecules that desorb above 723 K in He (0.62 $nm^{-2}$; Figure 4a); it represents the removal of all bound molecules retained after He treatment at 723 K by a DME chemical treatment at this same temperature. This areal density is much smaller than the number of Zr−O pairs at *m*-$ZrO_2$ surfaces (e.g., 7 $nm^{-2}$ for (001) and 11 $nm^{-2}$ for (011)),[60] indicating that a minority of sites bind $H_2O$ strongly and DME removes these titrants at much lower temperatures than does thermal desorption in He. These sites that bind $H_2O$ strongly are responsible for catalytic (de)hydrogenation reactivity.

He treatments at the higher temperatures required to desorb $H_2O$ from the strongest binding and most competent catalytic sites led to the sintering of *m*-$ZrO_2$ samples (130 $m^2$ $g^{-1}$ at 723 K to 33 $m^2$ $g^{-1}$ at 1108 K from $N_2$ uptakes) and significant crystal growth (9−35 nm for He treatments ranging from 723 to 1108 K). Crystallite sizes determined from surface areas (assuming spherical particles) agree well with those derived from diffraction line breadth (Figure S3; Supporting Information). Initial areal $C_3H_8$ dehydrogenation rates decreased with increasing He treatment temperatures (340 to 176 $\mu$mol $m^{-2}$ $h^{-1}$ for 723 and 1108 K treatments, respectively; Figure 4b), consistent with lower areal site densities on larger crystals. Indeed, areal site densities (from $H_2O$ titrations; Figure 4b and inset) decreased monotonically with increasing He treatment temperatures (0.55 sites $nm^{-2}$ at 723 K; 0.35 sites $nm^{-2}$ at 1108 K). Figure 4c shows that areal dehydrogenation rates decrease as $ZrO_2$ crystallites grow as a consequence of decreasing areal site densities. The increased prevalence of sites on smaller crystallites implicates the involvement of Zr−O site pairs at corners and edges, whose relative abundance is highest (per mass) for the smallest crystallites. The edge sites provide significant coordinative unsaturation (due to fewer bonds with other surface Zr and O atoms) that enables adsorbates to bind strongly. This allows these sites to stabilize bound $H_2O$ and the kinetically relevant TS for both hydrogenation and dehydrogenation (as described in Section 2.3 by DFT calculations). Their decrease with the He treatment temperature shows that such sites become less prevalent as crystallites grow.

Gravimetric hydrogenation and dehydrogenation rates reflect the number of sites per mass of catalysts, which, in turn, depends on the surface area and areal site density; both of these attributes decrease with increasing treatment temperatures. Site-normalized rates and rate constants are unaffected by treatment temperature and crystallite size (rate constants per site of 24 to 22 $h^{-1}$ $kPa^{-1}$ for treatments from 723 to 1108 K treatment; Figure 4c). These similar site reactivities indicate that the Zr−O pairs that form most of the products are similar in structure and reactivity, but different in number, over this range of treatment temperatures. These data also demonstrate that such sites are reliably probed during reaction using $H_2O$ as a quantitative titrant otherwise a variation in site reactivities would be evident and site densities from titration protocols would not match the $H_2O$ quantity desorbed during temperature increase protocols (Figure 4a). DME treatments preserve higher surface areas and areal site densities compared to He treatments at higher temperatures that remove the same quantity of $H_2O$. These combined contributions give rise to 100-fold higher rates over those obtained after He treatments at the same temperature (e.g., 723 K) for acyclic hydrogenation and dehydrogenation (Table 1).[6]

The measured site densities enable estimates of turnover rates of $C_3H_6$ hydrogenation reactions for benchmarking against those reported on dispersed metal nanoparticles. Rates are reported in Table 2 (per mass of catalyst and per site, when site counts or dispersions are reported) for catalysts based on Pd,[49,50] Pt,[51,52] Ni,[53] Ir,[54,55] Rh,[55−57] and Co[58] together with their respective reaction conditions. The entries in the table were selected from more than 40 reports (listed in Table S1; Supporting Information). Gravimetric $C_3H_6$ hydrogenation rates on these noble and transition metal catalysts range from $10^0$ to $10^5$ mol $kg^{-1}$ $min^{-1}$, typically at temperatures around 300 K to avoid deactivation processes typical at higher temperatures. The reported rate expressions are quite disparate among these previous studies and, in fact, are neither measured nor reported in most cases. When rate equations are reported, they exhibit diverse and mechanistically implausible fractional kinetic orders in reactant pressures, often with denominator terms that account for significant coverage of intermediates or spectators. These complex and contradictory kinetic trends reported for dispersed metals stand in contrast with the simple rate equations reported here for acyclic alkenes on LAB pairs, thus precluding benchmarking by bringing these reported rates to the conditions of the present study and requiring that the


https://doi.org/10.1021/acscatal.5c03523
ACS Catal. 2025, 15, 12610−12626

Scheme 1. Catalytic Cycle for $C_2H_4$ Hydrogenation on $ZrO_2$[a]

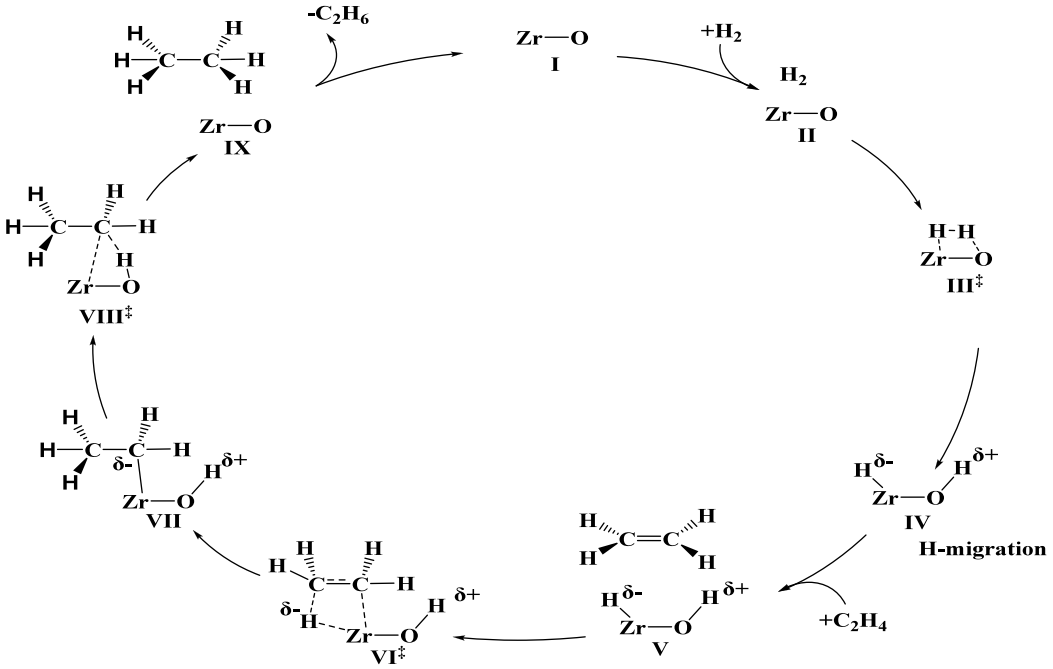


[a]Roman numerals correspond to the intermediates and TS species involved in the elementary steps.

rates of the present study be interpolated and extrapolated to the reported conditions.

To benchmark $m$-$ZrO_2$ against materials reported in the literature, the rate eq (eq 5) and temperature dependence of rates (Figure 2c) for $C_3H_6$ hydrogenation is used to calculate the gravimetric rates on DME-treated $m$-$ZrO_2$ at the temperatures and pressures reported for each literature catalyst (Table 2; details in Section S2; Supporting Information). The reports in Table 2 reflect the catalyst from each metal type that compared best to the predicted rates of $m$-$ZrO_2$. Gravimetric rates on $m$-$ZrO_2$ are slightly lower than those reported on Ni ($2.0 \times 10^5$ and $4.6 \times 10^5$ mol $kg^{-1}$ $min^{-1}$, respectively), but much higher than on Rh, Pt, Pd, Ir, or Co catalysts (by factors of 10 to $10^4$). Measured site densities of $m$-$ZrO_2$ were used to calculate turnover rates at the reported literature reaction conditions (Table 2). $C_3H_6$ hydrogenation turnover rate predictions on $m$-$ZrO_2$ catalysts treated by DME at 723 K were $5 \times 10^{-2} - 4.6 \times 10^4$ $s^{-1}$ over the range of temperatures (308−673 K) and reactant pressures (0.6−154 kPa) in literature reports. Turnover rates on Pd,[49,50] Pt,[51,52] and Co[58] catalysts reported in Table 2 were estimated from reported dispersions (by $H_2$ chemisorption or electron micrographs). Turnover rates were lower for each Pt-, Pd-, and Co-based catalyst (0.1 to 100 $s^{-1}$) than for $m$-$ZrO_2$ at the respective conditions (each ~$10^4$ $s^{-1}$). These turnover rates for DME-treated (723 K) $m$-$ZrO_2$, indicate the high intrinsic hydrogenation reactivity of these Zr−O LAB active sites. These comparisons show the potential practical relevance of earth-abundant $m$-$ZrO_2$ for the hydrogenation of acyclic alkenes.

DME treatments at 723 K uncover the most active sites for H−H cleavage and C−H formation in $C_3H_6$ (and other) hydrogenation reactions as well as for the respective dehydrogenation reactions. The unblocking of these active sites at temperatures below those required for titrant thermal desorption avoids the sintering and annealing of the catalyst. Their accessibility and the stability conferred by ensuring anhydrous and anaerobic conditions allow the kinetic evaluation required for assessments of the mechanism of their action in alkene hydrogenation based on elementary steps. The next sections extend from mechanistic insights informed by kinetic evaluation to theoretical and conceptual descriptions of alkene hydrogenation to determine the kinetic relevance of the elementary steps that mediate hydrogenation reactions and the lack of site coverage using DFT methods (Section 3.3). Energies derived from these DFT models demonstrate that forward and reverse reactions are mediated by a single kinetically relevant TS on bare sites, underscoring the thermodynamic links that connect the rate parameters and mechanism for hydrogenation and dehydrogenation reactions (Section 3.4).

**3.3. Identity and Kinetic Relevance of Elementary Steps in $C_2H_4$ and $C_3H_6$ Hydrogenation at Zr−O Pairs at $m$-$ZrO_2$(−111) Surfaces: DFT-Derived Energies of Bound Intermediates and Transition States.** The results described in Sections 3.1 and 3.2 indicate that Zr−O site pairs on $m$-$ZrO_2$ stabilize the kinetically relevant TS for hydrogenation and dehydrogenation reactions. Kinetic trends for hydrogenation (Section 3.1) and dehydrogenation[6] rates indicate that Zr−O LAB site pairs remain essentially free of bound species during catalytic turnovers; these catalytic cycles require the cleavage (or formation) of H−H bonds and the formation (or cleavage) of C−H bonds during each catalytic hydrogenation (dehydrogenation) turnover. Scheme 1 depicts a plausible sequence of elementary steps that is consistent with these data and their interpretation.

This sequence can be assessed using DFT methods and low-index $m$-$ZrO_2$(−111) surface models and specifically those pairs on the surface that bind $H_2O$ most strongly (described in Section 2.4). In this sequence, the Zr−O site pairs with open coordination (I, in Scheme 1) bind $H_2$ molecules (II) and dissociate them heterolytically via TS III‡ to form a cation−


https://doi.org/10.1021/acscatal.5c03523
ACS Catal. 2025, 15, 12610−12626

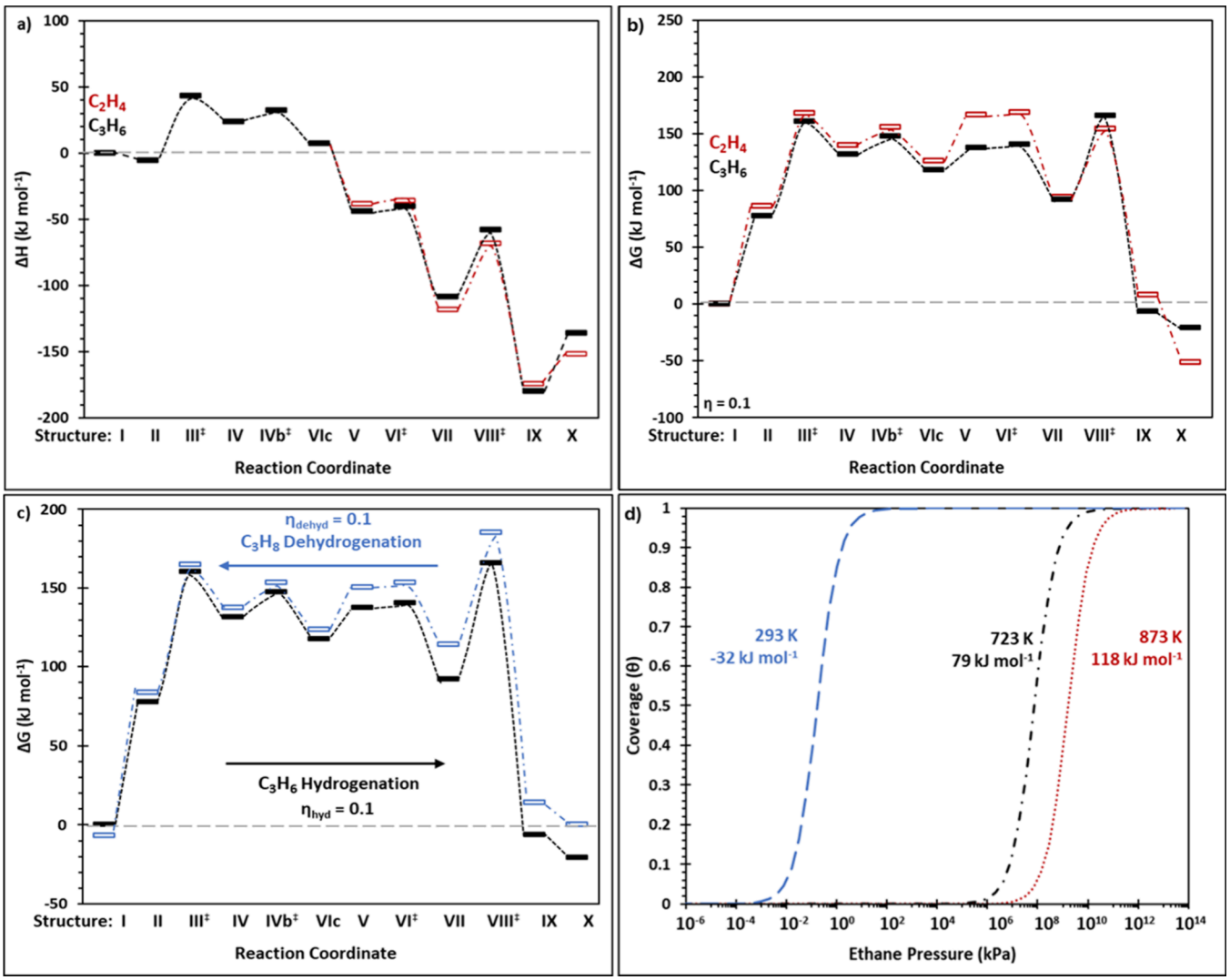


**Figure 5.** Reaction coordinate diagrams (723 K) for $C_2H_4$ (open red, -●-) and $C_3H_6$ hydrogenation (closed black, ---) showing the change in a) enthalpy and b) free energy for $\eta$ of 0.1. c) Free energy for $C_3H_6$ hydrogenation (closed black, ---) and $C_3H_8$ dehydrogenation (open blue, -●-) at 723 K and $\eta$=0.1 for each reaction. Species I is the reference state for hydrogenation while species X is the reference state for dehydrogenation. (d) Coverage of bound $C_3H_7^-$ (species VII) the $Zr_2{-}O_1$ LAB site pair of *m*-$ZrO_2$(−111) as a function of pressure at 293 K (blue, - - -), 723 K (black, -● -), and 873 K (red, ●●●) with the free energies of the species (1 bar, with respect to a bare site, $C_3H_{6(g)}$, and $H_{2(g)}$) labeled for reference.

anion pair interaction with the Zr and O atoms, respectively (IV). The hydridic species in IV migrates to a vicinal bridging Zr−H−Zr configuration, and the alkene binds weakly at the Zr center, which is made accessible by this $H^{\delta-}$ shift, to form V. The $H^{\delta-}$ species then forms a bond with a C atom in the alkene via TS VI$^{\ddagger}$ to form a loosely bound carbanion. The $H^{\delta+}$ then reacts with a C atom vicinal to that which reacted with $H^{\delta-}$ and is bound to Zr in a step mediated by TS VIII$^{\ddagger}$ to form the bound alkane (IX), which ultimately desorbs, yielding bare Zr−O site pair and thus completing a hydrogenation turnover.

DFT-derived enthalpies and free energies of the intermediates and transition states involved in these $C_2H_4$ and $C_3H_6$ hydrogenation elementary steps (Scheme 1) are used to assess their reversibility and kinetic relevance. These energies were determined at the $Zr_2{-}O_1$ LAB site pair in *m*-$ZrO_2$(−111) surfaces (depicted in Figure 1) because it shows the lowest coordination among exposed pairs and binds dissociated $H_2O$ most strongly ($\Delta H$: −132 kJ mol$^{-1}$) among all Zr−O pairs (−30 to −132 kJ mol$^{-1}$); the strong binding of $H_2O$ on active sites is expected from $H_2O$ titration of the most competent hydrogenation-dehydrogenation active sites (Figure 4b). Enthalpies (Figure 5a) and free energies (Figure 5b; 723 K; $\eta$: 0.1) of intermediates and TS in the sequence of elementary steps comprising a catalytic turnover are shown in Figure 5 and Table 3. All energies represent those for the formation of each moiety from gaseous $H_2$, the bare $Zr_2{-}O_1$ LAB site pair in *m*-$ZrO_2$(−111), and either $C_2H_4$ or $C_3H_6$ gaseous reactants for hydrogenation reactions (methods described in Section 2.4) or a gaseous alkane for dehydrogenation reactions. The geometries of the relevant intermediates and transition states are shown in Figure 6. Free energies depend substantially on the conditions ($P$ and $T$) for which they are evaluated. The relationship of free energy with temperature ($T$; 723 K here) is reflected in the T·S term in the free energy equation, but the specific pressures of reactants and products also substantially influence the free energy of product, reactant, and intermediate species, since entropy depends on pressure. The entropy for species $i$, $\Delta S_i$, at a given pressure ($P_1$) differs from that at the reference pressure (P; defined by convention, but otherwise arbitrarily as 1 bar) according to


https://doi.org/10.1021/acscatal.5c03523
ACS Catal. 2025, 15, 12610−12626

**Table 3. DFT-Derived Enthalpies ($\Delta H$) and Free Energies ($\Delta G$) of $C_2H_4$ ($_{C2}$) and $C_3H_6$ ($_{C3}$) Hydrogenation on *m*-$ZrO_2$(−111) at 723 K for $\eta$ = 0.1 at 1 bar Total Pressure**

| species | description | $\Delta H$ (kJ mol$^{-1}$) | $\Delta G^{\circ}_{\eta: 0.1}$ (kJ mol$^{-1}$) |
|---|---|---|---|
| $I_{C2}$ | $ZrO_{2,\ bare}$ | 0 | 0 |
| $II_{C2}$ | $ZrO_{2,\ H2*}$ | −6 | +86 |
| $III^{\ddagger}_{C2}$ | $(ZrO_{2,\ H2*})^{\ddagger}$ | 43 | 168 |
| $IV_{C2}$ | $ZrO_{2,\ 2H*}$ | +23 | +140 |
| $IVb^{\ddagger}_{C2}$ | $(ZrO_{2,\ 2H*})^{\ddagger}$ | 32 | 156 |
| $IVc_{C2}$ | $ZrO_{2,\ 2H*}$ | +7 | +126 |
| $V_{C2}$ | $ZrO_{2,\ C2H4-2H*}$ | −38 | +166 |
| $VI^{\ddagger}_{C2}$ | $(ZrO_{2,\ C2H4-2H*})^{\ddagger}$ | −36 | 169 |
| $VII_{C2}$ | $ZrO_{2,\ C2H5-H*}$ | −119 | +94 |
| $VIII^{\ddagger}_{C2}$ | $(ZrO_{2,\ C2H5-H*})^{\ddagger}$ | −68 | 154 |
| $IX_{C2}$ | $ZrO_{2,\ C2H6*}$ | −174 | +8 |
| $X_{C2}$ | $ZrO_{2,\ C2H6}$ | −152 | −51 |
| $I_{C3}$ | $ZrO_{2,\ bare}$ | 0 | 0 |
| $II_{C3}$ | $ZrO_{2,\ H2*}$ | −6 | +78 |
| $III^{\ddagger}_{C3}$ | $(ZrO_{2,\ H2*})^{\ddagger}$ | 43 | 161 |
| $IV_{C3}$ | $ZrO_{2,\ 2H*}$ | +23 | +132 |
| $IVb^{\ddagger}_{C3}$ | $(ZrO_{2,\ 2H*})^{\ddagger}$ | 32 | 148 |
| $IVc_{C3}$ | $ZrO_{2,\ 2H*}$ | +7 | +118 |
| $V_{C3}$ | $ZrO_{2,\ C3H6-2H*}$ | −44 | +138 |
| $VI^{\ddagger}_{C3}$ | $(ZrO_{2,\ C3H6-2H*})^{\ddagger}$ | −40 | 141 |
| $VII_{C3}$ | $ZrO_{2,\ C3H7-H*}$ | −109 | +92 |
| $VIII^{\ddagger}_{C3}$ | $(ZrO_{2,\ C3H7-H*})^{\ddagger}$ | −58 | 166 |
| $IX_{C3}$ | $ZrO_{2,\ C3H8*}$ | −180 | −6 |
| $X_{C3}$ | $ZrO_{2,\ C3H8}$ | −136 | −21 |

$$\Delta S_i = -R \times \ln(P_{i,1}/P_{i,\mathrm{ref}}) \quad (6)$$

where $P_{i,1}$ is the pressure of species *i*, which differs from the standard reference pressure of species *i*, $P_{\mathrm{ref}}$ (e.g., $P_{i,1}$: 0.01 bar, $P_{i,\mathrm{ref}}$: 1 bar). Lower gas-phase pressures increase *S* for gas-phase species, consequently decreasing *G*. Since only a fraction (e.g., 0.7; details inSection 2.4 and S1; Supporting Information) of the gas-phase entropies are retained upon adsorption of a gaseous molecule, lower pressures also cause a decrease G for surface-bound species, but to a smaller extent than for the gas-phase species to which they are referenced. This results in an overall increase in formation-free energies ($\Delta G^{\circ}$) for bound species. In contrast, lower product pressures (for a given reactant pressure) lead to lower free energies of bound product-like species since the $S_{\mathrm{product}}$ increases, but the reference reactant entropy is unchanged. This decrease in free energy of product-like species as their pressure decreases enables reactions to proceed in directions consistent with thermodynamics (i.e., $\eta$ < 1 gives spontaneous forward reactions). The recognition that relative pressures influence the free energy landscape led to the use of an $\eta$ value of 0.1 (total pressure of 1 bar) to assess the reaction coordinate at conditions consistent with experimental assessments to most accurately compare DFT results to the measured kinetics.

$C_3H_6$ hydrogenation turnovers require $H_2$ dissociation and the reaction of both H atoms in $H_2$ with the two C atoms in the alkene C=C bond. H−H cleavage proceeds via molecular adsorption ($\Delta H$: −6 kJ mol$^{-1}$; $\Delta G^{\circ}$: + 78 kJ mol$^{-1}$, $\Delta G^{\circ}$ is the formation free energy at 723 K for $\eta$ = 0.1 with respect to a bare site, and gaseous $H_2$ and $C_3H_6$) at locations distant from the Zr−O site pair where dissociation occurs (2.7 Å from the Zr atom; species II). Dissociation occurs by placing one H at the Zr atom (1.9 Å; H−Zr distance) and the other one at the O atom (0.97 Å; O−H) (species IV). The formation enthalpy of these fragments is +23 kJ mol$^{-1}$ and the free energy is unfavorable ($\Delta G^{\circ}$: + 132 kJ mol$^{-1}$), indicative of surface coverages that are kinetically undetectable at all reaction conditions (e.g., < $10^{-7}$ fractional coverage H* at 1 bar $H_2$ and 723 K), as inferred from rate data (eq 5). This $H^{\delta+}$−$H^{\delta-}$ pair (Species IV) forms via TS III$^{\ddagger}$ with an enthalpy of 43 kJ mol$^{-1}$ ($\Delta G^{\ddagger}$: 161 kJ mol$^{-1}$) from gaseous reactants and a bare Zr−O pair. The $H^{\delta-}$ species subsequently migrates to a bridging location between the $Zr_1$ and $Zr_2$ atoms (IVc; Scheme 1) via TS IVb$^{\ddagger}$ with a TS formation enthalpy and free energy of 32 and 148 kJ mol$^{-1}$, respectively. The product state, with $H^{\delta+}$ at the O atom and $H^{\delta-}$ at the Zr−H−Zr bridge (IVc), is slightly more stable than IV ($\Delta H$: + 7 kJ mol$^{-1}$; $\Delta G^{\circ}$: + 118 kJ mol$^{-1}$). Bader charges show that H−H dissociation proceeds heterolytically (+0.57 and −0.52 e for the H atoms bound at the O atom and at the $Zr_1$−$Zr_2$ bridge position, respectively. This displacement of $H^{\delta-}$ provides sufficient open coordination for interactions with $C_3H_6$ at the LAB site pair.

The $C_3H_6$ molecule binds at the LAB site pair after $H^{\delta-}$ migration to the $Zr_1$−$Zr_2$ bridge position (3.0 Å nearest C atom to Zr distance) via species V ($\Delta H$: −44 kJ mol$^{-1}$; $\Delta G$: + 138 kJ mol$^{-1}$). The first C−H bond formation reaction can occur at either the terminal or internal C atom in the C=C bond in $C_3H_6$ (the two C atoms in $C_2H_4$ are identical). Either $H^{\delta+}$ (bound to $O_1$) or $H^{\delta-}$ (bound between $Zr_1$ and $Zr_2$) adds to the terminal (to form *n*-$C_3H_7$) or the internal (to form *i*-$C_3H_7$) C atoms in bound $C_3H_6$ via TS VI$^{\ddagger}$. $H^{\delta-}$ addition from $Zr_1$−H-$Zr_2$ to the secondary C atom of $C_3H_6$ in VI$^{\ddagger}$ forms *n*-$C_3H_7$ species bound to $Zr_1$ (VII) with a TS formation enthalpy of −40 kJ mol$^{-1}$ and a free energy of 141 kJ mol$^{-1}$. The formation enthalpy of VII is −109 kJ mol$^{-1}$ (ΔG: + 92 kJ mol$^{-1}$). Bader charges confirmed that the charge from $H^{\delta-}$ (−0.52 in V) is transferred to the Zr-bound *n*-$C_3H_7$, during the formation of TS VI$^{\ddagger}$; the latter shows a −0.47 charge (at species VII), consistent with the anionic character of this alkyl fragment and with the absence of any net transfer of charge to the Zr−O site pair. The charge at the $H^{\delta+}$ fragment bound at the O atoms remains unchanged during the formation of the alkyl anion.

An alternate route in which $H^{\delta-}$ adds to the terminal C atom in $C_3H_6$ to form a bound *i*-$C_3H_7$ anion involves a TS with a formation-free energy that is 23 kJ mol$^{-1}$ larger than that for the formation of *n*-$C_3H_7$. As a result, the addition of $H^{\delta-}$ to the secondary C atom in $C_3H_6$ to form *n*-$C_3H_7$ is the more facile route. If instead the cationic $H^{\delta+}$ fragment adds to either C atom in $C_3H_6$, a cationic alkyl species (*n*-$C_3H_7^{\delta+}$: + 0.76 e; *i*-$C_3H_7^{\delta+}$: + 0.7 e) forms at the O atom in the LAB site pair. Again, no net transfer of charge occurs to either the Zr or the O atom. These alternate routes are enthalpically disfavored over those leading to alkyl anions (by +44 kJ mol$^{-1}$ for *n*-$C_3H_7^{\delta+}$ and +36 kJ mol$^{-1}$ for *i*-$C_3H_7^{\delta+}$). The product state free energy of the addition of $H^{\delta+}$ to $C_3H_6$ is also less favorable than that of $H^{\delta-}$ addition routes (higher by +53 kJ mol$^{-1}$ for *n*-$C_3H_7^{\delta+}$ and +39 kJ mol$^{-1}$ for *i*-$C_3H_7^{\delta+}$). These enthalpies and free energies indicate that the addition of the anionic H-fragment ($H^{\delta-}$) to the methylene C atom in bound $C_3H_6$, with the formation of an*n*-$C_3H_7^{\delta-}$ species, is the preferred route for the formation of the first C−H bonds in $C_3H_6$ hydrogenation.

Hydrogenation turnovers require subsequent reactions of $H^{\delta+}$ with *n*-$C_3H_7^{\delta-}$ to form gaseous $C_3H_8$ products. In this step, the terminal $CH_2$ group in *n*-$C_3H_7^{\delta-}$ weakens its interaction with the Zr atom as it incipiently reacts with $H^{\delta+}$


https://doi.org/10.1021/acscatal.5c03523
ACS Catal. 2025, 15, 12610−12626

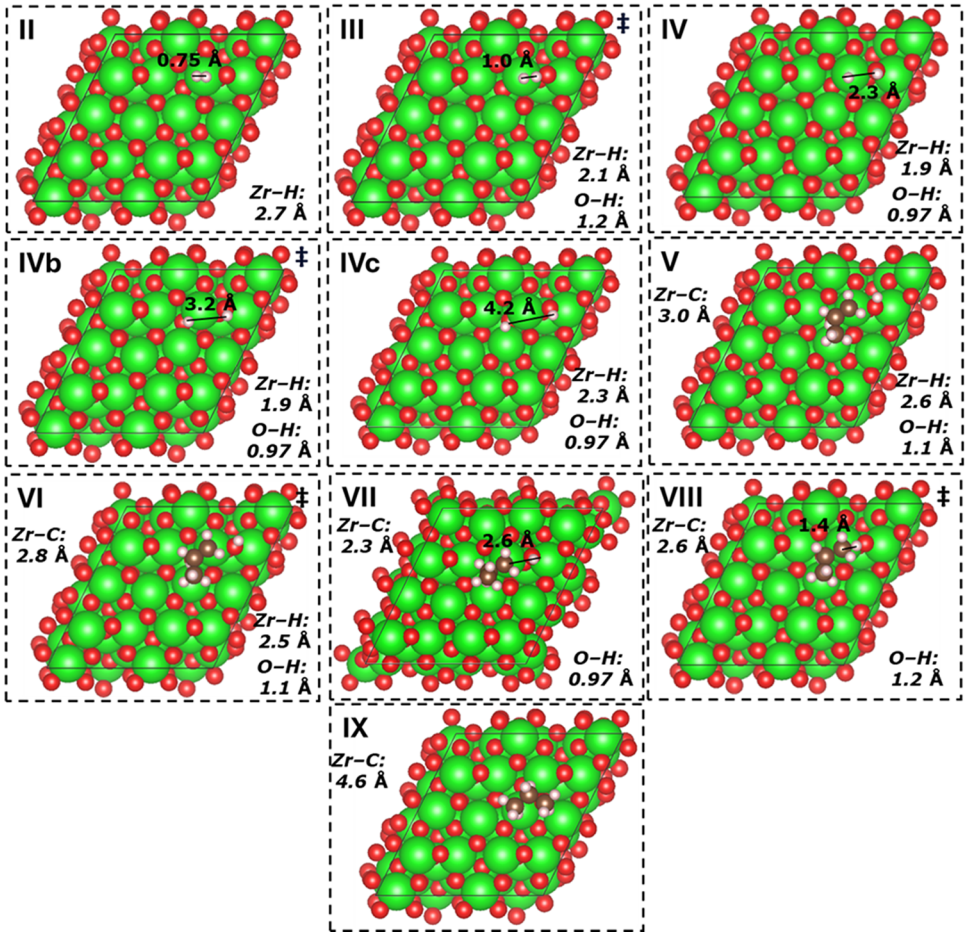


**Figure 6.** Space-filling representations of DFT-optimized structures for intermediates and TS of $C_3H_6$ and $H_2$ in hydrogenation on *m*-$ZrO_2$(−111) and select bond lengths. Zr: green; O: red; C: brown; H: white.

to form a bound $C_3H_8$ molecule. This step is mediated by TS VIII$^‡$, with a formation free energy of 166 kJ mol$^{-1}$ ($\Delta H^‡$: −58 kJ mol$^{-1}$); the formation enthalpy of bound $C_3H_8$ (Species IX) is −180 kJ mol$^{-1}$ ($\Delta G$: −6 kJ mol$^{-1}$). The final step desorbs weakly bound $C_3H_8$, a step that reforms the bare site and $C_3H_8(g)$ (species X) with a formation enthalpy of −136 kJ mol$^{-1}$ ($\Delta G$: −21 kJ mol$^{-1}$), a value in agreement with the heat and free energies of reaction for $C_3H_6$ hydrogenation (−130 kJ mol$^{-1}$; $\Delta G°_{723\ K}$: −27.4 kJ mol$^{-1}$). These positive free energies along the $C_3H_6$ hydrogenation reaction coordinate indicate that no species bind strongly to Zr−O site pairs, consistent with experimental assessments. The energy profile can also be used to identify key elementary steps that inhibit rates by limiting the turnover frequency; the kinetic relevance of elementary steps is discussed next.

The kinetic relevance of elementary steps is determined by the formation of the TS with the highest free energy along the reaction coordinate. The kinetically relevant step is not, in general, the step with the highest enthalpy barrier, but its corresponding enthalpy dictates the measured temperature dependence of rates (apparent activation energy). The highest free energy along the reaction coordinate for $C_3H_6$ hydrogenation corresponds to TS VIII$^‡$, which mediates the $H^{\delta+}$ addition to form $C_3H_8$ ($\Delta G^‡$: 166 kJ mol$^{-1}$); this free energy barrier agrees well with measured activation free energies derived from site-normalized rate constants ($\Delta G^‡$: 158 kJ mol$^{-1}$). The measured activation energy (−48 ± 2 kJ mol$^{-1}$, Figure 2c) is consistent with DFT-derived enthalpies of formation (−58 kJ mol$^{-1}$) for the kinetically relevant TS in $C_3H_6$ hydrogenation when the reactant state consists of a bare LAB site pair and the two gaseous reactants; this reference state is dictated by hydrogenation rates that are proportional to both alkene and $H_2$ pressures (Figure 2b).

Forward hydrogenation reactions are favored, by definition, when the corresponding $\eta$ is less than unity, consistent with Le Chatelier's principle, but the kinetic relevance of steps may shift with temperature ($T$) and pressure ($P$) because of their concomitant effects on the free energies of reactants, products, and TS for different elementary steps along the reaction coordinate. Those effects for $C_3H_6$ hydrogenation are shown in Figure S4 (Supporting Information) at $\eta$ = 0.01, 0.1, 1, and 10. Higher $\eta$ values lead to higher free energies of product-like species and higher reaction free energies. For $\eta > 1$, the overall reaction favors the reverse dehydrogenation path, but TS VIII$^‡$ remains the highest free energy barrier across this wide range of conditions ($\eta$). The unwavering kinetic relevance of steps mediated by TS VIII$^‡$ indicates that both hydrogenation and dehydrogenation share the interconversion of $H^{\delta+}$ and *n*-$C_3H_7^{\delta-}$ with $C_3H_8$ as the sole kinetically relevant step and that other elementary steps can be treated as quasi-equilibrated.

The kinetic relevance of steps mediated by TS VIII$^‡$ in both forward and reverse directions over a wide range of conditions (at least $0.01 < \eta < 10$; shown in Figure S4; Supporting Information) is supported by the free energy landscapes of the


https://doi.org/10.1021/acscatal.5c03523
ACS Catal. 2025, 15, 12610−12626

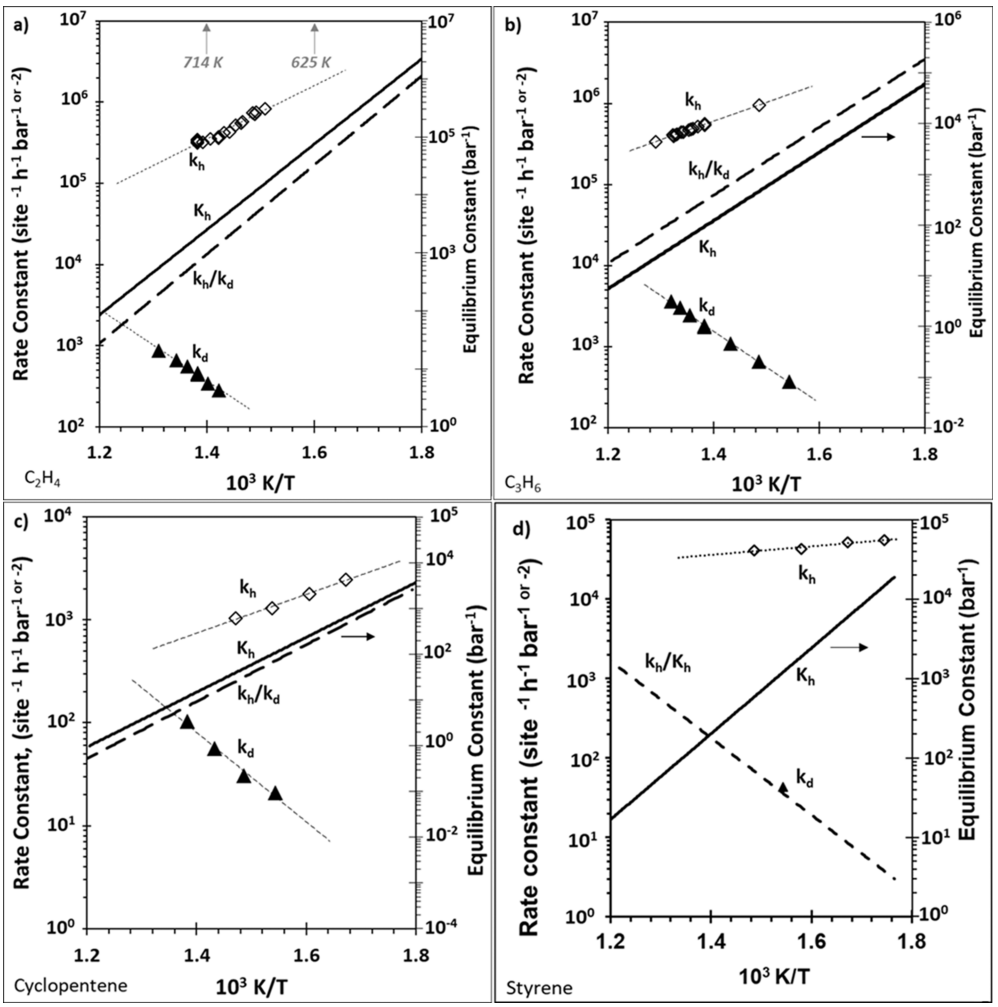


**Figure 7.** Rate constants for (a) $C_2H_4$ hydrogenation ($k_h$, open diamonds, dashed line indicating exponential regression, 52 ± 9 kJ mol$^{-1}$) and $C_2H_6$ dehydrogenation ($k_d$, closed triangles, dashed line indicating exponential regression, 84 ± 7 kJ mol$^{-1}$), (b) $C_3H_6$ hydrogenation (−48 ± 2 kJ mol$^{-1}$) and $C_3H_8$ dehydrogenation (84 ± 3 kJ mol$^{-1}$), (c) cyclopentene hydrogenation (−39 kJ mol$^{-1}$) and cyclopentane dehydrogenation (83 ± 8 kJ mol$^{-1}$), and (d) styrene hydrogenation (−10 ± 3 kJ mol$^{-1}$) and ethylbenzene dehydrogenation, with comparisons of equilibrium constants (solid lines) to the ratio of $k_h/k_d$ (dashed lines, a−c). The dashed line in (d) instead predicts $k_d$ from $k_h/K_h$.

reaction coordinate diagram in Figure 5c, which shows both $C_3H_6$ hydrogenation and $C_3H_8$ dehydrogenation at an $\eta$ value of 0.1 for their respective reactions. The selection of $\eta$ enforces thermodynamic favorability in their respective forward directions, and TS VIII$^{‡}$ exhibits the highest free energy of formation among all TS for both hydrogenation and dehydrogenation. The kinetic relevance of this step was shown previously for alkane dehydrogenation.[6] Additionally, the free energies of all bound intermediates remain positive across both reaction profiles, consistent with Zr−O pairs that remain essentially unoccupied throughout the reactions—a prerequisite for kinetic trends governed by the overall stoichiometry in either direction. The difference in DFT-derived activation enthalpies for $C_3H_6$ hydrogenation (−58 kJ mol$^{-1}$) and $C_3H_8$ dehydrogenation (78 kJ mol$^{-1}$) is 136 kJ mol$^{-1}$, closely matching the overall reaction enthalpy (130 kJ mol$^{-1}$). The involvement of a single kinetically relevant step at bare Zr−O site pairs also accounts for the close correspondence between the forward/reverse rate constant ratios and equilibrium constants at each temperature (see Section 3.4). Although such consistency is generally attributed to the principle of microscopic reversibility only at equilibrium, De Donder relations may be applied even under nonequilibrium conditions when: (i) a single kinetically relevant step mediated by a shared transition state governs both directions, and (ii) the surface remains essentially bare throughout. Having established the kinetic relevance of VIII$^{‡}$ for both reactions, the evidence supporting the persistence of bare surface sites under all conditions is next examined.

The kinetic relevance of specific elementary steps can shift as surfaces become populated by intermediates. Langmuirian adsorption treatments of intermediate species' free energies ($\eta$ of 0.01, the 1 bar condition) were used to estimate surface coverages of all intermediates for $C_3H_6$ hydrogenation (free energies in Table S2; Supporting Information). Positive formation free energies are evident for nearly every intermediate state except for that of bound $C_3H_8$ in species IX (−21 kJ mol$^{-1}$), which favorably desorbs to form a bare site (−35 kJ mol$^{-1}$). The preeminence of bare sites is shown by the expected coverage of the next most stable bound intermediate (anionic alkyl species of VII) over a range of pressures ($10^{-6}$–$10^{14}$ kPa) and temperatures (293−873 K) shown in Figure 5d. Active sites remain essentially bare at relevant pressures (e.g., 1 kPa) and higher temperatures (723 and 873 K), consistent


https://doi.org/10.1021/acscatal.5c03523
ACS Catal. 2025, 15, 12610−12626

with experimental assessments. At temperatures <293 K, the free energy is sufficiently low (−32 kJ mol$^{-1}$) to enable detectable coverage at 1 kPa, but the barrier for H-insertion is also substantially decreased at these conditions ($\Delta G^{\ddagger}$: 17 kJ mol$^{-1}$). The weak binding of hydrocarbons over a wide range of conditions results in sites that remain essentially bare also under reaction conditions, as suggested by the kinetic rate expressions consistent with the law of mass action on *m*-$ZrO_2$.

DFT-derived enthalpies and free energies ($\eta$: 0.1) for the hydrogenation of $C_2H_4$ were likewise assessed. The energies of all steps, intermediates, and transition states are shown in Table 3, and the DFT-derived overall reaction enthalpy (−152 kJ mol$^{-1}$) is consistent with gas-phase thermochemistry (−142 kJ mol$^{-1}$).[61] Figure 5a,b depicts the enthalpy and free energy (723 K) reaction coordinate profiles for $C_2H_4$ hydrogenation. These profiles indicate high barriers for $H_2$ dissociation (III$^{\ddagger}$; $\Delta H^{\ddagger}$: 43; $\Delta G^{\ddagger}$: 168 kJ mol$^{-1}$), the first H-addition step (VI$^{\ddagger}$; $\Delta H^{\ddagger}$: −36; $\Delta G^{\ddagger}$: 169 kJ mol$^{-1}$), and the second H-addition step (VIII$^{\ddagger}$; $\Delta H^{\ddagger}$: −68; $\Delta G^{\ddagger}$: 154 kJ mol$^{-1}$). The free energies of these TS are similar, suggesting that the kinetic relevance of steps for $C_2H_4$ hydrogenation may be more sensitive to the experimental conditions. The consistency of the formation enthalpy of the second H-addition TS, VIII$^{\ddagger}$ (−68 for $C_2H_4$ hydrogenation), and the experimentally assessed activation enthalpy (−52 ± 9 kJ mol$^{-1}$), implicate it as kinetically relevant at the conditions of our experiments.

The $C_3H_6$ hydrogenation reaction coordinate diagrams at $0.01 < \eta < 10$ show that TS VIII$^{\ddagger}$ is the sole kinetically relevant step along the reaction coordinate for both hydrogenation and dehydrogenation reactions at 723 K. Formation free energies at conditions corresponding to 1 bar of each gaseous species are commonly used to assess kinetic relevance, but this treatment neglects both the thermodynamic preference of the reaction and the effect that such pressures have on the formation free energies of TS species. Without further model manipulations, this typically used *standard* convention only discriminates the kinetically relevant step if all reactants and products were present at 1 bar, seldom the case in either academic or practical reaction conditions. The kinetic relevance of TS VIII$^{\ddagger}$, the interconversion of *n*-$C_3H_7^{\delta-}$ and $C_3H_8$, at 1 bar of all species ($\eta$: 0.01) is reasonable in this case only because it is true for a wide range of conditions, including those where dehydrogenation reactions prevail ($\eta$: 10). Both hydrogenation and dehydrogenation reactions occur on Zr−O site pairs that essentially remain devoid of bound species across a wide range of temperatures and pressures, and the activation enthalpies indicate that there are thermodynamic links between the kinetics of the two reactions. The next section demonstrates these thermodynamic links by assessing the kinetics of forward and reverse reactions of acyclic, cyclic, and pendant side chains of arenes.

**3.4. Thermodynamic Links between Hydrogenation of Unsaturated Hydrocarbons and Reverse Hydrocarbon Dehydrogenation.** Kinetic trends for the hydrogenation of $C_2H_4$, $C_3H_6$, and cyclopentene and their respective reverse dehydrogenation reactions all reflect the corresponding reaction stoichiometries. Further, the relationship between measured rate constants for forward and reverse reactions is demonstrated for $C_2H_4$, $C_3H_6$, and cyclopentene. Rate constants for hydrogenation reactions (per active site, 573−773 K) are shown in Figure 7 for $C_2H_4$, $C_3H_6$, cyclopentene, and styrene. These hydrogenation rate constants decrease with increasing temperature, indicating that the TS is lower in enthalpy than the reactant state (unsaturated hydrocarbon, $H_2$, and the bare surface). In contrast, dehydrogenation rate constants increase with temperature. The ratio of the Arrhenius dependencies of forward and reverse rate constants ($k_h/k_d$) was evaluated for each reaction pair, and this ratio reflects the equilibrium constant of the corresponding reaction (within a factor of 2.5). The relative rate constants for *i*-$C_4H_8$ hydrogenation and *i*-$C_4H_{10}$ dehydrogenation also appear to conform to these relations, but this was not extensively investigated. The equivalence of the ratio of rate constants and the equilibrium constant indicates that the free energies of each reaction pair are related by gas-phase reaction thermodynamics as prescribed by DeDonder relations:[62]

$$K_h = e^{-(\Delta G^{\circ})/RT} = \frac{k_h}{k_d} \tag{7}$$

The relationship is further reflected in the van't Hoff dependence of equilibrium constants on temperatures (eqs S13−S16; Supporting Information), demonstrated for $C_2H_4$, $C_3H_6$, and cyclopentene hydrogenation. The activation enthalpies for $C_2H_4$, $C_3H_6$, cyclopentene, and styrene are −52 ± 9, −48 ± 2, −39 ± 4, and −10 ± 3 kJ mol$^{-1}$, respectively. Rate constants for reverse reactions of $C_2H_6$, $C_3H_8$, and cyclopentene dehydrogenation obey the law of mass action and exhibit activation barriers of 84 ± 7, 84 ± 3, and 83 ± 8 kJ mol$^{-1}$, respectively. The difference in measured barriers of hydrogenation and dehydrogenation for each set of reactions (136, 132, and 122 kJ mol$^{-1}$, for $C_2H_6$, $C_3H_8$, and cyclopentane, respectively) matches well to the heat of reaction for each reaction pair (142, 130, and 115 kJ mol$^{-1}$, respectively). These thermodynamic links indicate that De Donder formalisms[64] can be extended beyond elementary steps at equilibrium to an entire catalytic pathway mediated by concerted interactions on active site pairs if the following three conditions are satisfied: (i) forward and reverse pathways each obey the law of mass action and (ii) both forward and reverse reactions occur on active sites devoid of significant coverage of intermediate species, and (iii) these forward and reverse reactions are mediated by a sole kinetically relevant step. These criteria were verified by measured reaction kinetics that obey the law of mass action and indicate bare sites under the conditions of both reactions as well as by DFT-based assessments of the reaction pathways, which demonstrated that sites remain bare and identified the common kinetically relevant TS in both reaction directions (over a wide range of conditions). The resulting rate constant ratios for forward and reverse reactions consequently yield the equilibrium constant. This evidence indicates that the rate relations governed by microscopic reversibility can be applied to this whole catalytic sequence, even if they are far from equilibrium conditions. Previous work on acidic zeolites with isolated active sites showed that it is possible to accurately predict rates of the forward−reverse reaction pairs in alkene hydrogenation from measured rates of one reaction using thermodynamic links,[62,63] but the present study demonstrates that such relations can be applied to heterolytic activation processes at site pairs far from equilibrium, enabling accurate predictions of reverse reaction rates from thermodynamics if forward reaction rates are known.

The predictive capabilities were deployed to assess the viability of industrially significant reactions of the pendant chains of arenes. Styrene hydrogenation was used as a


https://doi.org/10.1021/acscatal.5c03523
ACS Catal. 2025, 15, 12610−12626

representative example due to the commercial relevance and potential competence of the reverse reaction of ethylbenzene dehydrogenation, used in practice to produce styrene as a monomer for plastics synthesis.[65] The hydrogenation of styrene was carried out on DME-treated $m$-$ZrO_2$ at 573−673 K. The hydrogenation rates are directly proportional to styrene and $H_2$ pressures and they decreased with increasing temperature with an apparent activation barrier of −10 kJ $mol^{-1}$. Rates of ethylbenzene dehydrogenation were estimated on DME-treated $m$-$ZrO_2$ by using hydrogenation rate constants and the gas-phase heat of reaction (126 kJ $mol^{-1}$). The predictions in the large, dashed line of Figure 7d ($k_h/K_h$) reflect dehydrogenation rate constants that are similar to those of other alkane dehydrogenation reactions shown above. This prediction was confirmed by a reaction of ethylbenzene on $m$-$ZrO_2$ at 648 K (closed triangle; Figure 7d), showing promise for the LAB site pairs of nonreducible oxides as alternative catalysts for ethylbenzene dehydrogenation, as well as the rigorous nature of these predictive capabilities. Comprehensive testing of DME-treated $m$-$ZrO_2$ for ethylbenzene dehydrogenation and its potential practical relevance are the subject of ongoing investigation. The accurate prediction of dehydrogenation or hydrogenation rates from the reverse reaction through relations with thermodynamics is a powerful tool for screening potential applications of a catalyst for a broad range of reactions.

These results demonstrate that the removal of bound titrants from the surfaces of earth-abundant oxide catalysts using DME treatments uncovers the most competent Zr−O LAB sites for hydrogenation reactions of alkenes, cycloalkenes, and arene pendant side chains. Such treatments also increase the reactivity of LAB-based catalysts for the reverse reactions of alkane, cycloalkane, and arene pendant side chain dehydrogenation to the same extent. The active sites are minority LAB site pairs that possess an invariant intrinsic reactivity irrespective of particle size, surface area, or site density for a given catalyst. These Zr−O site pairs must remain devoid of $H_2O$ or $CO_2$ titrants to keep sites available for catalysis since they strongly bind these titrants, thus requiring anhydrous and anaerobic conditions for the target catalytic reactions. These sites do not strongly bind hydrocarbon species and, therefore, remain bare during reactions. Because the forward and reverse reactions both follow the law of mass action and proceed through a single, kinetically relevant C−H activation step, De Donder relations can be applied to show that alkene (and cycloalkene or arene side chain) hydrogenation and alkane (or cycloalkane or arene side chain) dehydrogenation have rate constants linked by gas-phase thermodynamics. This relationship holds even under conditions far from equilibrium and provides a powerful predictive tool for evaluating plausible reactions on these uniquely active, earth-abundant oxides.

## 4. CONCLUSIONS

The catalytic competency of $m$-$ZrO_2$ for hydrogenation of alkenes, cycloalkenes, and arene pendant chains is demonstrated by employing chemical treatments with DME that react with hydroxyl groups to expose the most active Lewis acid−base (LAB) site pairs. Chemical treatments preserve surface area typically lost during high-temperature $H_2O$ desorption protocols and enhance hydrogenation rates by up to 2 orders of magnitude, enabling kinetic analysis on these otherwise inaccessible sites. Both hydrogenation and the corresponding dehydrogenation reactions obey the law of mass action and exhibit first-order kinetics with respect to reactant pressures, consistent with a surface free of hydrocarbon-derived species during turnover. Negative apparent activation energies for hydrogenation suggest transition states (TS) that are enthalpically stabilized relative to gas-phase reactants. Moreover, the difference in activation barriers between forward and reverse reactions matches the enthalpy of the reaction, directly linking kinetics to thermodynamic driving forces.

Quantitative titration with $H_2O$ reveals an active site density of 0.56 $nm^{-2}$ for $m$-$ZrO_2$ treated at 723 K, confirming that catalytically competent LAB pairs represent a minority of surface Zr−O motifs. These sites persist under rigorously anhydrous and anaerobic conditions, sustaining high turnover frequencies that rival or exceed those of noble metals and other transition metal catalysts. Mechanistic interpretations from kinetic data, supported by DFT, indicate that hydrogenation proceeds via heterolytic H−H activation and a sole kinetically relevant C−H bond-forming step at undercoordinated Zr−O pairs. Importantly, the reversible interconversion between surface-bound $n$-$C_3H_7^{\delta-}$ and $C_3H_8$ governs both hydrogenation and dehydrogenation rates and this kinetic relevance preserved over a wide range of conditions ($0.01 < \eta < 10$ and beyond).

Because both forward and reverse reactions occur on the same bare sites via the same TS and adhere to mass action kinetics, the De Donder relations apply to the full catalytic sequence, even under conditions far from equilibrium. This framework enables the predictive determination of rate constants for alkane and cycloalkane dehydrogenation from measured rates of their corresponding hydrogenation reactions using only gas-phase thermodynamics. This approach was extended to accurately predict ethylbenzene dehydrogenation rates from styrene hydrogenation data, positioning $m$-$ZrO_2$ as a promising alternative to state-of-the-art ethylbenzene dehydrogenation catalysts. More broadly, these findings not only reframe the role of metal oxides in selective hydrogenation but also establish a thermodynamically grounded predictive framework for (de)hydrogenation kinetics. The ability of LAB sites to activate X−H bonds (X = H, C, and O) further suggests that these earth-abundant materials could be broadly applicable in non-noble metal catalysis for selective bond activation.

## ■ ASSOCIATED CONTENT

### Supporting Information

The Supporting Information is available free of charge at https://pubs.acs.org/doi/10.1021/acscatal.5c03523.

(S.1) Calculation of enthalpies and entropies using statistical mechanics formalisms; (S.2) comparison of $C_3H_6$ hydrogenation with reported catalysts based on precious metals; (S.3) supporting experimental data; (S.4) supporting computational data (PDF)

## ■ AUTHOR INFORMATION

### Corresponding Author

**Enrique Iglesia** − *Department of Chemical and Biomolecular Engineering, University of California at Berkeley, Berkeley, California 94720, United States; Davidson School of Chemical Engineering, Purdue University, West Lafayette, Indiana 47907, United States;* orcid.org/0000-0003-4109-1001; Email: iglesia@berkeley.edu



https://doi.org/10.1021/acscatal.5c03523
ACS Catal. 2025, 15, 12610−12626

## Authors

**Nicholas R. Jaegers** − *Department of Chemical and Biomolecular Engineering, University of California at Berkeley, Berkeley, California 94720, United States;* orcid.org/0000-0002-9930-7672

**Mikalai Artsiusheuski** − *Department of Chemical and Biomolecular Engineering, University of California at Berkeley, Berkeley, California 94720, United States;* orcid.org/0000-0003-4931-9568

**Vardan Danghyan** − *Department of Chemical and Biomolecular Engineering, University of California at Berkeley, Berkeley, California 94720, United States*

**Junnan Shangguan** − *Department of Chemical and Biomolecular Engineering, University of California at Berkeley, Berkeley, California 94720, United States*

**Carlos Lizandara-Pueyo** − *BASF SE, Ludwigshafen am Rhein 67056, Germany;* orcid.org/0000-0003-1146-775X

Complete contact information is available at: https://pubs.acs.org/10.1021/acscatal.5c03523


## Notes

The authors declare the following competing financial interest(s): The authors have filed provisional patent applications for the catalyst compositions and methods of preparation, pretreatment protocols of metal oxides for alkane dehydrogenation and alkene hydrogenation reactions, and for reactant stream purification protocols.

## ■ ACKNOWLEDGMENTS

This research used resources of the National Energy Research Scientific Computing Center (NERSC), a U.S. Department of Energy Office of Science User Facility located at Lawrence Berkeley National Laboratory, operated under contract no. DE-AC02-05CH11231 using NERSC award ERCAP0023779. We acknowledge BASF for financial support and technical guidance through the California Research Alliance.

## ■ REFERENCES


(1) Vilé, G.; Albani, D.; Almora-Barrios, N.; López, N.; Pérez-Ramírez, J. Advances in the Design of Nanostructured Catalysts for Selective Hydrogenation. *ChemCatChem.* **2016**, *8*, 21−33.

(2) Burwell, R. L., Jr. Supported Platinum, Palladium, and Rhodium Catalysts. *Langmuir* **1986**, *2*, 2−11.

(3) Minachev, K. M.; Khodakov, Y. S.; Nakhshunov, V. S. Hydrogenation of Alkenes on Oxide Catalysts. *Russ. Chem. Rev.* **1976**, *45*, 142.

(4) Cain-Borgman, C. J.; Danghyan, V.; Jaegers, N.; Lizandara Pueyo, C.; Dellamorte, J. C.; Kundu, A.; Shangguan, J.; Iglesia, E. Lewis Acid Base Pairs as Highly Active Catalytic Sites for Hydrogenation and Dehydrogenation Processes. USPTO: 2024016500, WO2024177986A2 **2023**.

(5) Iglesia, E.; Shangguan, J. Pretreating Metal Oxide Catalysts for Alkane Dehydrogenation. USPTO: 20230303465, WO2022132843A1 **2022**.

(6) Jaegers, N.; Danghyan, V.; Shangguan, J.; Lizandara-Pueyo, C.; Deshlahra, P.; Iglesia, E. Heterolytic C-H Activation Routes in Catalytic Dehydrogenation of Light Alkanes on Lewis Acid-Base Pairs at Zro2 Surfaces. *J. Am. Chem. Soc.* **2024**, *146*, 25710−25726.

(7) Tanabe, K. Surface and Catalytic Properties of Zro2. *Mater. Chem. Phys.* **1985**, *13*, 347−364.

(8) Nakano, Y.; Yamaguchi, T.; Tanabe, K. Hydrogenation of Conjugated Dienes over Zro2 by H2 and Cyclohexadiene. *J. Catal.* **1983**, *80*, 307−314.

(9) Wang, W.; et al. Single Co Sites in Ordered Sio2 Channels for Boosting Nonoxidative Propane Dehydrogenation. *ACS Catal.* **2022**, *12*, 2632−2638.

(10) Wu, L.; Ren, Z.; He, Y.; Yang, M.; Yu, Y.; Liu, Y.; Tan, L.; Tang, Y. Atomically Dispersed Co2+ Sites Incorporated into a Silicalite-1 Zeolite Framework as a High-Performance and Coking-Resistant Catalyst for Propane Nonoxidative Dehydrogenation to Propylene. *ACS Appl. Mater. Interfaces* **2021**, *13*, 48934−48948.

(11) Hu, B.; Kim, W.-G.; Sulmonetti, T. P.; Sarazen, M. L.; Tan, S.; So, J.; Liu, Y.; Dixit, R. S.; Nair, S.; Jones, C. W. A Mesoporous Cobalt Aluminate Spinel Catalyst for Nonoxidative Propane Dehydrogenation. *ChemCatChem.* **2017**, *9*, 3330−3337.

(12) Searles, K.; Siddiqi, G.; Safonova, O. V.; Copéret, C. Silica-Supported Isolated Gallium Sites as Highly Active, Selective and Stable Propane Dehydrogenation Catalysts. *Chem. Sci.* **2017**, *8*, 2661−2666.

(13) Cybulskis, V. J.; Pradhan, S. U.; Lovón-Quintana, J. J.; Hock, A. S.; Hu, B.; Zhang, G.; Delgass, W. N.; Ribeiro, F. H.; Miller, J. T. The Nature of the Isolated Gallium Active Center for Propane Dehydrogenation on Ga/Sio2. *Catal. Lett.* **2017**, *147*, 1252−1262.

(14) Tanabe, K.; Yamaguchi, T. Acid-Base Bifunctional Catalysis by Zro2 and Its Mixed Oxides. *Catal. Today* **1994**, *20*, 185−197.

(15) Li, W.; Huang, H.; Li, H.; Zhang, W.; Liu, H. Facile Synthesis of Pure Monoclinic and Tetragonal Zirconia Nanoparticles and Their Pahse Effects on the Behavior of Supported Molybdena Catalysts for Methanol Seletive Oxidation. *Langmuir* **2008**, *24*, 8358−8366.

(16) Price, G. L.; Iglesia, E. Matrix Method for Correction of Mass Spectra in Deuterium-Exchange Applications. *Industrial & engineering chemistry research* **1989**, *28*, 839−844.

(17) Kresse, G.; Furthmuller, J. Efficient Iterative Schemes for Ab Initio Total-Energy Calculations Using a Plane-Wave Basis Set. *Phys. Rev. B* **1996**, *54*, 11169−11186.

(18) Perdew, J. P.; Burke, K.; Ernzerhof, M. Generalized Gradient Approximation Made Simple. *Phys. Rev. Lett.* **1996**, *77*, 3865−3868.

(19) Grimme, S.; Ehrlich, S.; Goerigk, L. Effect of the Damping Function in Dispersion Corrected Density Functional Theory. *J. Comput. Chem.* **2011**, *32*, 1456−1465.

(20) Kresse, G.; Joubert, D. From Ultrasoft Pseudopotentials to the Projector Augmented-Wave Method. *Physical review b* **1999**, *59*, 1758.

(21) Monkhorst, H. J.; Pack, J. D. Special Points for Brillouin-Zone Integrations. *Phys. Rev. B* **1976**, *13*, 5188−5192.

(22) Henkelman, G.; Uberuaga, B. P.; Jónsson, H. A Climbing Image Nudged Elastic Band Method for Finding Saddle Points and Minimum Energy Paths. *J. Chem. Phys.* **2000**, *113*, 9901−9904.

(23) Henkelman, G.; Uberuaga, B. P.; Jonsson, H. A Climbing Image Nudged Elastic Band Method for Finding Saddle Points and Minimum Energy Paths. *J. Chem. Phys.* **2000**, *113*, 9901−9904.

(24) Henkelman, G.; Jonsson, H. Improved Tangent Estimate in the Nudged Elastic Band Method for Finding Minimum Energy Paths and Saddle Points. *J. Chem. Phys.* **2000**, *113*, 9978−9985.

(25) Henkelman, G.; Jónsson, H. A Dimer Method for Finding Saddle Points on High Dimensional Potential Surfaces Using Only First Derivatives. *J. Chem. Phys.* **1999**, *111*, 7010−7022.

(26) Monkhorst, H. J.; Pack, J. D. Special Points for Brillouin-Zone Integrations. *Phys. Rev. B* **1976**, *13*, 5188.

(27) Wang, S.; Iglesia, E. Substituent Effects and Molecular Descriptors of Reactivity in Condensation and Esterification Reactions of Oxygenates on Acid-Base Pairs at Tio2 and Zro2 Surfaces. *J. Phys. Chem. C* **2016**, *120*, 21589−21616.

(28) Jain, A.; Ong, S. P.; Hautier, G.; Chen, W.; Richards, W. D.; Dacek, S.; Cholia, S.; Gunter, D.; Skinner, D.; Ceder, G.; Persson, K. A. Commentary: The Materials Project: A Materials Genome Approach to Accelerating Materials Innovation. *APL Mater.* **2013**, *1*, No. 011002.

(29) Zhang, Y.; Zhao, Y.; Otroshchenko, T.; Lund, H.; Pohl, M. M.; Rodemerck, U.; Linke, D.; Jiao, H.; Jiang, G.; Kondratenko, E. V. Control of Coordinatively Unsaturated Zr Sites in Zro 2 for Efficient C-H Bond Activation. *Nat. Commun.* **2018**, *9*, 3794.

(30) Hofmann, A.; Clark, S. J.; Oppel, M.; Hahndorf, I. Hydrogen Adsorption on the Tetragonal Zro 2 (101) Surface: A Theoretical Study of an Important Catalytic Reactant. *Phys. Chem. Chem. Phys.* **2002**, *4*, 3500−3508.
(31) Haase, F.; Sauer, J. The Surface Structure of Sulfated Zirconia: Periodic Ab Initio Study of Sulfuric Acid Adsorbed on Zro2 (101) and Zro2 (001). *J. Am. Chem. Soc.* **1998**, *120*, 13503−13512.
(32) Christensen, A.; Carter, E. A. First-Principles Study of the Surfaces of Zirconia. *Phys. Rev. B* **1998**, *58*, 8050.
(33) Morterra, C.; Cerrato, G.; Ferroni, L.; Negro, A.; Montanaro, L. Surface Characterization of Tetragonal Zro2. *Appl. Surf. Sci.* **1993**, *65*, 257−264.
(34) Zhang, Y.; Zhao, Y.; Otroshchenko, T.; Han, S.; Lund, H.; Rodemerck, U.; Linke, D.; Jiao, H.; Jiang, G.; Kondratenko, E. V. The Effect of Phase Composition and Crystallite Size on Activity and Selectivity of Zro2 in Non-Oxidative Propane Dehydrogenation. *J. Catal.* **2019**, *371*, 313−324.
(35) Wu, H.; Duan, Y.; Liu, K.; Lv, D.; Qin, L.; Shi, L.; Tang, G. First-Principles Study of Phase Transition and Band Structure of Zro2 under Pressure. *J. Alloys Compd.* **2015**, *645*, 352−357.
(36) Korhonen, S. T.; Calatayud, M.; Krause, A. O. I. Stability of Hydroxylated (111) and (101) Surfaces of Monoclinic Zirconia: A Combined Study by Dft and Infrared Spectroscopy. *J. Phys. Chem. C* **2008**, *112*, 6469−6476.
(37) Hofmann, A.; Sauer, J. Surface Structure of Hydroxylated and Sulfated Zirconia. A Periodic Density-Functional Study. *J. Phys. Chem. B* **2004**, *108*, 14652−14662.
(38) French, R. H.; Glass, S.; Ohuchi, F.; Xu, Y.-N.; Ching, W. Experimental and Theoretical Determination of the Electronic Structure and Optical Properties of Three Phases of Zro 2. *Phys. Rev. B* **1994**, *49*, 5133.
(39) Howard, C.; Hill, R.; Reichert, B. Structures of Zro2 Polymorphs at Room Temperature by High-Resolution Neutron Powder Diffraction. *Acta Crystallographica Section B: Structural Science* **1988**, *44*, 116−120.
(40) Ruh, R.; Corfield, P. W. Crystal Structure of Monoclinic Hafnia and Comparison with Monoclinic Zirconia. *J. Am. Ceram. Soc.* **1970**, *53*, 126−129.
(41) Momma, K.; Izumi, F. Vesta 3 for Three-Dimensional Visualization of Crystal, Volumetric and Morphology Data. *J. Appl. Crystallogr.* **2011**, *44*, 1272−1276.
(42) McQuarrie, D. *Statistical Mechanics*; University Science Books: Sausalito, CA, 2000; pp 222−223.
(43) Sprowl, L. H.; Campbell, C. T.; Árnadóttir, L. Hindered Translator and Hindered Rotor Models for Adsorbates: Partition Functions and Entropies. *J. Phys. Chem. C* **2016**, *120*, 9719−9731.
(44) Deshlahra, P.; Iglesia, E. Methanol Oxidative Dehydrogenation on Oxide Catalysts: Molecular and Dissociative Routes and Hydrogen Addition Energies as Descriptors of Reactivity. *J. Phys. Chem. C* **2014**, *118*, 26115−26129.
(45) Deshlahra, P.; Iglesia, E. Reactivity and Selectivity Descriptors for the Activation of C-H Bonds in Hydrocarbons and Oxygenates on Metal Oxides. *J. Phys. Chem. C* **2016**, *120*, 16741−16760.
(46) Johnson, R. D. III Nist Standard Reference Database Number 101. In *NIST Computational Chemistry Comparison and Benchmark Database*; NIST: Gaithersburg, 2022. http://cccbdb.nist.gov/ (accessed 2022−04−04).
(47) Cramer, C. J. *Essentials of Computational Chemistry: Theories and Models*; Wiley: 2005; p 618.
(48) Xu, M.; Lunsford, J. H.; Goodman, D. W.; Bhattacharyya, A. Synthesis of Dimethyl Ether (Dme) from Methanol over Solid-Acid Catalysts. *Applied Catalysis A: General* **1997**, *149*, 289−301.
(49) Brandão, L.; Fritsch, D.; Madeira, L. M.; Mendes, A. M. Kinetics of Propylene Hydrogenation on Nanostructured Palladium Clusters. *Chem. Eng. J.* **2004**, *103*, 89−97.
(50) Rogers, G. B.; Lih, M. M.; Hougen, O. A. Catalytic Hydrogenation of Propylene and Isobutylene over Platinum. *Effect of Noncompetitive Adsorption. Aiche J.* **1966**, *12*, 369−377.
(51) Salnikov, O. G.; Kovtunov, K. V.; Barskiy, D. A.; Bukhtiyarov, V. I.; Kaptein, R.; Koptyug, I. V. Kinetic Study of Propylene Hydrogenation over Pt/Al2o3 by Parahydrogen-Induced Polarization. *Appl. Magn. Reson.* **2013**, *44*, 279−288.
(52) Ortiz-Soto, L. B.; Monnier, J. R.; Amiridis, M. D. Structure-Sensitivity of Propylene Hydrogenation over Cluster-Derived Bimetallic Pt-Au Catalysts. *Catal. Lett.* **2006**, *107*, 13−17.
(53) Carturan, G.; Enzo, S.; Ganzerla, R.; Lenarda, M.; Zanoni, R. Role of Solid-State Structure in Propene Hydrogenation with Nickel Catalysts. *Journal of the Chemical Society, Faraday Transactions* **1990**, *86*, 739−746.
(54) Argo, A. M.; Odzak, J. F.; Goellner, J. F.; Lai, F. S.; Xiao, F. S.; Gates, B. C. Catalysis by Oxide-Supported Clusters of Iridium and Rhodium: Hydrogenation of Ethene, Propene, and Toluene. *J. Phys. Chem. B* **2006**, *110*, 1775−1786.
(55) Weber, W. A.; Zhao, A.; Gates, B. C. Nay Zeolite-Supported Rhodium and Iridium Cluster Catalysts: Characterization by X-Ray Absorption Spectroscopy During Propene Hydrogenation Catalysis. *J. Catal.* **1999**, *182*, 13−29.
(56) Zhao, H.; Hsiao, L.-Y.; Rudawski, N. G.; Song, B.; Kuan, P.-C.; Hullender, L.; Hagelin-Weaver, H. Influence of Tio2 Structure on Metal-Support Interactions in Rh/Tio2 Catalysts Probed by Propylene Hydrogenation and Other Techniques. *Appl. Surf. Sci.* **2024**, *654*, No. 159389.
(57) Pinna, F.; Candilera, C.; Strukul, G.; Bonivento, M.; Graziani, M. Catalytic Hydrogenation of Propene over Polymer Supported Rhodium Complexes. *J. Organomet. Chem.* **1978**, *159*, 91−98.
(58) Aaserud, C.; Hilmen, A.-M.; Bergene, E.; Eric, S.; Schanke, D.; Holmen, A. Hydrogenation of Propene on Cobalt Fischer−Tropsch Catalysts. *Catal. Lett.* **2004**, *94*, 171−176.
(59) Schweitzer, N. M.; Hu, B.; Das, U.; Kim, H.; Greeley, J.; Curtiss, L. A.; Stair, P. C.; Miller, J. T.; Hock, A. S. Propylene Hydrogenation and Propane Dehydrogenation by a Single-Site Zn2+ on Silica Catalyst. *ACS Catal.* **2014**, *4*, 1091−1098.
(60) Piskorz, W.; Gryboś, J.; Zasada, F.; Cristol, S.; Paul, J.-F.; Adamski, A.; Sojka, Z. Periodic Dft and Atomistic Thermodynamic Modeling of the Surface Hydration Equilibria and Morphology of Monoclinic Zro2 Nanocrystals. *J. Phys. Chem. C* **2011**, *115*, 24274−24286.
(61) Yaws, C. L. *The Yaws Handbook of Physical Properties for Hydrocarbons and Chemicals*; Elsevier: 2015.
(62) Gounder, R.; Iglesia, E. Catalytic Hydrogenation of Alkenes on Acidic Zeolites: Mechanistic Connections to Monomolecular Alkane Dehydrogenation Reactions. *J. Catal.* **2011**, *277*, 36−45.
(63) Yun, J. H.; Lobo, R. F. Radical Cation Intermediates in Propane Dehydrogenation and Propene Hydrogenation over H-[Fe] Zeolites. *J. Phys. Chem. C* **2014**, *118*, 27292−27300.
(64) Donder, D.; Rysselberghe, V. *Thermodynamic Theory of Affinity*; Standford University Press: 1936.
(65) Oliveira, A. C.; Fierro, J. L. G.; Valentini, A.; Nobre, P. S. S.; do Carmo Rangel, M. Non-Toxic Fe-Based Catalysts for Styrene Synthesis: The Effect of Salt Precursors and Aluminum Promoter on the Catalytic Properties. *Catal. Today* **2003**, *85*, 49−57.


https://doi.org/10.1021/acscatal.5c03523
*ACS Catal.* 2025, 15, 12610−12626